RESEARCH ARTICLE

Preparation of PANI modified TiO$_2$ and characterization under pre- and post- photocatalytic conditions

Nazli Turkten[1] · Yunus Karatas[1] · Ceyda S. Uyguner-Demirel[2] · Miray Bekbolet[2]

Abstract

Polyaniline (PANI) is a promising conducting polymer for surface modification of TiO$_2$ to overcome limitations of the use of visible light and attain increased photocatalytic efficiency for the removal of organic contaminants. In this study, a series of polyaniline modified TiO$_2$ (PANI-TiO$_2$) composites were prepared by using "*in-situ*" chemical oxidation polymerization method. The composites were systematically characterized by Fourier transform infrared spectroscopy (equipped with an attenuated total reflection accessory, FTIR-ATR), Raman spectroscopy, X-ray diffractometry (XRD), scanning electron microscopy coupled with energy dispersive X-ray spectroscopy (SEM-EDAX), X-ray photoelectron spectroscopy (XPS), ultraviolet–visible diffuse reflectance spectroscopy (UV-DRS), photoluminescence spectroscopy (PL), nitrogen (N$_2$) physisorption (Brunauer − Emmett − Teller surface area (S$_{BET}$) and Barrett-Joyner-Halenda (BJH) pore size analysis), thermogravimetry-derivative thermogravimetry (TG-DTG) techniques. XRD patterns of PANI-TiO$_2$ composites confirmed both the amorphous phase of PANI and the crystalline character of TiO$_2$. TG/DTG analysis complemented the XRD profiles that the interactions between PANI and TiO$_2$ resulted in a more stable PANI-TiO$_2$ matrix. SEM images displayed the dominant morphology as dandelion-like shapes of PANI being more pronounced with increasing PANI ratios in PANI-TiO$_2$ composites. UV-DRS profiles revealed that the band gap energies of the composites were lower than bare TiO$_2$ expressing a shift to the visible light region. Both PL and UV-DRS analyses confirmed the band-gap reduction phenomenon of PANI modification of TiO$_2$. The incorporation of PANI into TiO$_2$ resulted in a reduction of the surface area of TiO$_2$. The composites were subsequently subjected to photocatalytic activity assessment tests using humic acid (HA) as a model of refractory organic matter (RfOM) under simulated solar irradiation (Uyguner-Demirel et al. Environ Sci Pollut Res 30 85626-85638, 2023). The morphological and structural changes attained upon application of photocatalysis were also evaluated by FTIR-ATR, Raman spectroscopy, XRD, and SEM-EDAX methods in a comparable manner. The FTIR-ATR spectral features of PANI, RfOM and all composites displayed peaks with slight shifts under pre- and post- photocatalytic conditions as well as following dark surface interactions. Besides exhibiting noticeable photocatalytic performance, PANI-TiO$_2$ composites were also proven to maintain stability under non-selective oxidation conditions in the presence of a complex organic matrix. The prepared PANI-TiO$_2$ composites overcoming the limitations of UVA light active bare TiO$_2$ photocatalysis could possibly find a beneficial use as potential catalysts in solar photocatalytic applications.

Keywords PANI-TiO$_2$ composites · Photocatalysis · Refractory organic matter · Surface modification

Responsible Editor: George Z. Kyzas

✉ Nazli Turkten
    nazli.turkten@yahoo.com

1   Department of Chemistry, Faculty of Arts and Sciences, Kirsehir Ahi Evran University, Kirsehir 40100, Türkiye

2   Institute of Environmental Sciences, Bogazici University, Bebek, Istanbul 34342, Türkiye

Introduction

Over the last few decades, heterogeneous photocatalysis has been demonstrated as an alternative advanced oxidation process in the area of water and wastewater treatment (Fujishima and Honda 1972; Nakata and Fujishima 2012; Wang et al. 2022). As an n-type semiconductor, TiO$_2$ is the most extensively studied photocatalyst in relation to its unique properties such as high oxidizing capability, photoactivity, chemical stability, low toxicity, and low-cost (Porcu

et al. 2022; Rehman et al. 2022). The main disadvantage of TiO$_2$ is the necessity of utilizing UV light due to the band gap energy levels of phases (anatase: $E_{bg} = 3.2$ eV and rutile: $E_{bg} = 3.0$ eV). To overcome this major drawback and to extent the utilization of TiO$_2$ efficiently under solar light irradiation, various strategies such as metal ion doping (*e.g.,* Fe, Cu, Mo), non-metallic ion doping (*e.g.,* C, N, S), noble-metal deposition (*e.g.,* Pt, Pd), co-doping (*e.g.,* N-S) and surface sensitization by organic dyes (*e.g.,* Ru(II) complexes) have been developed (Emeline et al. 2012; Pawar et al. 2023). Furthermore, polymeric composites are considered as appropriate candidates to enhance photocatalytic activity that could possibly extend the light absorption range to the visible region along with improvements in adsorption capacities (Enesca and Cazan 2022; Li et al. 2020; Oyetade et al. 2022). In this regard, recent interest is devoted to the modification of TiO$_2$ using conducting polymers (CPs) such as polyaniline (PANI), polythiophene, poly-(o-phenylene-diamine), polypyrrole, and their derivatives (Reddy et al. 2015; Singh et al. 2013; Turkten et al. 2021).

As one of the most studied CP, PANI comprised of an extended π-conjugated electron system expresses various physico-chemical properties *i.e.,* insolubility and stability in aqueous medium (Das et al. 2022; Singh and Shukla 2020). PANI homopolymer contains benzenoid and quinoid units in a sequence order or both units in different proportions. PANI is mainly synthesized via a chemical oxidation method in an acidic solution using aniline (ANI) monomer. In general, low-cost chemical synthesis of PANI is carried out using an oxidizing agent such as ammonium persulfate (APS), benzoyl peroxide, cerium(IV) sulfate, iron(III) chloride, hydrogen peroxide, manganese(IV) oxide, potassium dichromate, potassium periodate, potassium permanganate, potassium persulfate, silver nitrate and sodium perchlorate (Bhandari 2018; Bláha et al. 2017). Among these oxidants, APS is reported as a preferential oxidant revealing high polymerization yields (Turkten et al. 2021). In this acidic process (pH < 2.5), various inorganic acids (*e.g.,* hydrochloric acid, sulfuric acid, phosphoric acid, and hydrofluoric acid) and organic acids (*e.g.,* acetic acid, citric acid, and succinic acid) have been widely used as dopants (Eftekhari 2010; Stejskal 2020; Wan 2008).

Although *in-situ* oxidation polymerization is the most preferred PANI-TiO$_2$ preparation method, different approaches have also been reported such as; UV-light mediated green synthesis (Cionti et al. 2020), mixing (Lee et al. 2020; Wang et al. 2010), one-pot chemical oxidation polymerization (Wang et al. 2019), template-free method (Jumat et al. 2017) and direct impregnation (Sboui et al. 2017). Various oxidizing agents such as orthoperiodic acid (Doğan et al. 2020) and iron(III) chloride (Sambaza et al. 2020), along with different dopants such as sulfuric acid (Gilja et al. 2017; Radoičić et al. 2012; Rahman and Kar

2020a, b; Subramanian et al. 2014) and citric acid (Jeong et al. 2014) were also employed. Depending on the preparation methodology, PANI-TiO$_2$ composites exhibited different morphological and functional properties. Particularly, the synthesis of PANI-TiO$_2$ composites could be realized via *in-situ* oxidation polymerization of ANI using APS as an oxidizing agent and hydrochloric acid as a dopant (Deng et al. 2016; Gu et al. 2012a; Guo et al. 2014; Koysuren and Koysuren 2019; Radoičić et al. 2013; Reddy et al. 2016; Sandikly et al. 2021; Yang et al. 2017).

Turkten and colleagues performed a thorough literature survey revealing numerous studies on the preparation and characterization of PANI-TiO$_2$, followed by activity assessment tests using various substrates comprised of simple organics and mostly dyes as model compounds (Turkten et al. 2021). Based on these findings, this study was designed to prepare PANI-TiO$_2$ composites, to elucidate respective physicochemical, photophysical and morphological properties followed by activity assessment using a specific organic matrix under solar irradiation. To achieve this dual goal, a series of PANI-TiO$_2$ composites were prepared by *in-situ* oxidation polymerization method with varying ANI/TiO$_2$ mole ratios using APS as an oxidizing agent and HCl as a dopant. The photocatalyst specimens were characterized by well-defined methods. Accordingly, Fourier transform infrared spectroscopy (equipped with an attenuated total reflection accessory (FTIR-ATR), Raman spectroscopy, X-ray diffractometry (XRD), scanning electron microscopy coupled with energy dispersive X-ray spectroscopy (SEM-EDAX), X-ray photoelectron spectroscopy (XPS), ultraviolet–visible diffuse reflectance spectroscopy (UV-DRS), photoluminescence spectroscopy (PL), N$_2$ physisorption, thermogravimetry-derivative thermogravimetry (TG-DTG) techniques were applied systematically.

Following preparation and in-depth characterization of PANI-TiO$_2$ composites, solar light-initiated photocatalytic activities were assessed by using humic acid as a model of refractory organic matter (RfOM). RfOM represents organic matrix of low biodegradability mainly derived from degradation and repolymerization of aquatic and/or terrestrial matter (Frimmel et al. 2008). Generally, humic matter is defined as composed of an aromatic/aliphatic skeleton including carboxylic, phenolic, enolic, and alcoholic functional groups with a variety of different molecular weight sub-fractions. The polydisperse nature, ill-defined structure and complex composition of humic matter completely divert from the well-defined simple organics that are used as model compounds. During solar photocatalysis, humic matter and PANI both simultaneously acting as photosensitizers, quenchers of reactive oxygen species as well as hole scavengers could display diverse roles on the degradation pathway and kinetics of organic matrix. In this respect, the photocatalytic performances of the PANI-TiO$_2$ composites

were concomitantly reported by using RfOM UV–vis and fluorescence spectrophotometric parameters as well as mineralization extents (Uyguner-Demirel et al. 2023). As a complementary approach, under pre- and post-photocatalytic conditions, the composites were further characterized the results of which were also presented herein in a comparative manner.

Accordingly, the dual purpose of the study would be accomplished and PANI-TiO$_2$ composite could be introduced as a noticeable visible-light active photocatalyst specimen. Therefore, the elucidation of solar photocatalysis of "PANI-TiO$_2$ and RfOM" ternary system would provide significant information on the applicability of the composites.

Methodology

Materials

Titanium dioxide (TiO$_2$, P-25 grade, Evonik) was used as the primary photocatalyst and referred to simply as TiO$_2$. Aniline (ANI, C$_6$H$_5$NH$_2$, for analysis), ammonium persulfate (APS, (NH$_4$)$_2$S$_2$O$_8$ ACS reagent, $\geq$ 98.0%), and hydrochloric acid (HCl, ACS reagent, 37%) were provided by Merck and used without further purification. Humic acid (HA) was purchased from Aldrich as the sodium salt. All aqueous solutions were prepared with deionized water (conductivity < 1 µS/cm at 25 °C).

Preparation of PANI-TiO$_2$ Composites

PANI-TiO$_2$ composites were synthesized by *in-situ* chemical oxidation polymerization method proposed by Li and colleagues (Li et al. 2008a). The initial mole ratio of ANI/APS was 1:1 in all composites. The selected mole ratios of ANI/TiO$_2$ were 1:8, 1:4, 1:1, 4:1, and 8:1 and these composites were denoted as PT-18, PT-14, PT-11, PT-41, and PT-81, respectively. The representative synthesis of PT-11 was given as follows: Solution A was prepared by dissolving 17.13 g (75 mmol) of APS in 240 mL of 1 M HCl solution and placed in a dropping funnel. Solution B was prepared by adding 6.0 g (75 mmol) of TiO$_2$ to 240 mL of 1 M HCl solution in a flat-bottomed flask and the resulting slurry was subjected to ultrasonication for 15 min. Solution B was placed in an ice bath and 6.99 g (75 mmol) of ANI was added slowly via vigorous stirring provided by a magnetic stirrer. Solution A was added dropwise (approximately one drop/second) into solution B. Continuous stirring was provided for another 24 h at room temperature to ensure complete polymerization. Finally, the precipitate of the PANI-TiO$_2$ composite (PT-11) was filtered through a Gooch funnel equipped with a

sintered glass disc, extensively washed with first distilled water then ethanol, and dried in an air oven at 80 °C for at least 24 h until a constant weight was reached. The same procedure was also followed for the synthesis of bare PANI in the absence of TiO$_2$.

Characterization of PANI, TiO$_2$ and PANI-TiO$_2$ Composites

FTIR-ATR spectroscopy was performed using Thermo Scientific Nicolet 6700 Spectrometer. All spectra were recorded with 32 scans at a resolution of 4 cm^{-1} in the range of 4000–500 cm^{-1}. Dispersive Raman spectroscopic measurements were carried out by a Thermo Scientific DXR Raman Microscope with a spectral resolution of 2 cm^{-1}. Composites were excited using Ar$^+$ laser power (10 mW) at $\lambda = 532$ nm. Raman spectra for all specimens involved the average accumulation of five scans of 2 s per scan. XRD patterns were obtained by a Rigaku-D/MAX-Ultima diffractometer with Cu Kα radiation ($\lambda = 1.54$ Å) as X-ray source. The accelerating voltage and the applied current were 40 kV and 40 mA, respectively. The diffraction intensity was measured in the range of 5–80° with a scanning rate of 2° min^{-1}. Crystallite sizes (D, nm) of TiO$_2$ and PANI-TiO$_2$ composites were calculated using the Scherrer equation (Eq. 1) with reference to the reflection related to (1 1 0) and (2 0 0) planes of anatase TiO$_2$.

$$D = K\lambda/(\beta\cos\theta) \tag{1}$$

where K = 0.9, λ is the X-ray wavelength (1.5418 Å), θ is the Bragg angle, and β is the full width at half maximum intensity (FWHM, radians) (Scherrer 1918).

Spurr and Myers equation (Eq. 2) was used to determine the weight fractions of anatase and rutile phases.

$$f_A = 1/(1 + 1.26 I_R/I_A) \tag{2}$$

where f_A is the weight fraction of anatase phase, I_R and I_A denote the reflection intensities of rutile (1 1 0) and anatase (1 0 1) planes, respectively (Spurr and Myers 1957).

The lattice constants "a" and "c" of TiO$_2$ were determined from two appropriate reflections *i.e.,* (h k l) using the below given Eqs. 3 and 4 (Cullity and Stock 2014):

$$1/d^2 = [(h^2 + k^2)/a^2] + (1^2/c^2) \tag{3}$$

where k is the X-ray wavelength equal to 1.5418 Å for Cu Kα radiation and h is in radians. The value of d (lattice spacing, nm) for an XRD peak can be determined from 2θ angle by Braggs Law using the following equation:

$$d = \lambda/2\sin\theta \tag{4}$$

The peak positions (2θ) of anatase (1 0 1) and (2 0 0) reflections of TiO_2 were used to determine the lattice parameters.

SEM-EDAX analysis was performed on FEI-Philips XL30 Environmental Scanning Electron Microscope with Field Emission Gun and equipped with Energy Dispersive X-ray Analysis Unit. The prepared composite powders were supported on carbon tape and the instrument was operated at an accelerating voltage of 10 kV. XPS features were determined on a Thermo Scientific K-Alpha X-ray Photoelectron Spectrometer with a hemispherical electron analyzer and Al-K micro-focused monochromater. XPS survey spectra were acquired using a monochromated Al Kα X-ray source ($h\nu = 1486.6$ eV) with a pass energy of 150 eV and 0.1 eV step. For each specimen, an X-ray spot of ~400 μm radius was employed. All peak energies were calibrated to the binding energy of adventitious carbon as 284.6 eV. UV-DRS profiles were obtained using a Shimadzu UV-2401 PC instrument. The analysis range was from 190 to 800 nm and $BaSO_4$ was used as the reference material. PL spectra were acquired on an Edinburgh Instruments FS5 spectrofluorometer with an excitation wavelength at λ = 325 nm. BET method was used to calculate the specific surface area (S_{BET}) and Barrett-Joyner-Halenda method was used to determine the pore size distribution. The N_2 physisorption measurements were carried out at 77 K using a Quantachrome Quadrosorb SI instrument. Prior to the analysis, the specimens were degassed under vacuum at 80 °C for 18 h. The thermal treatment of PANI and PANI-TiO_2 composites was carried out by using a simultaneous TG-DSC instrument (PerkinElmer model STA 600) in the temperature range of 30 to 800 °C under an inert pure N_2 atmosphere with 20 mL/min flow rate and 10 °C/min heating rate.

Characterization of PANI and PANI-TiO₂ Composites following Photocatalysis

Photocatalytic degradation experiments were performed using an ATLAS Suntest CPS + simulator. Xenon lamp (250 W/m², wavelength range 300–800 nm) with a light intensity of $I_o = 1.67$ μE/min as determined by ferrioxalate actinometry was used as the light source (Hatchard and Parker 1956). 100 kDa molecular size fraction of HA was used as the representative of RfOM. Organic matrix was characterized by UV–vis and fluorescence spectroscopic parameters and dissolved organic carbon contents. Detailed information on RfOM preparation, characterization and photocatalytic experiments was explained elsewhere as the complementary part of this study (Uyguner-Demirel et al. 2023). Pre-adsorptive interactions prevailing between RfOM and specimens prior to photocatalysis were expressed as initial adsorption conditions. A certain amount of PANI or PANI/TiO_2 specimen (0.25 mg/mL) was introduced to RfOM solution and

sonicated to ensure complete dispersion. Dry specimens were obtained by filtration of the whole solution (50 mL) through a Millipore 0.22 μm membrane filter, and the filtrate was dried at 80 °C in an air oven. In order to maintain similar light exposure conditions, samples were subjected to photocatalytic treatment for a certain irradiation period ($t_{irr} = 60$ min). Dry samples were attained as described above. FTIR-ATR and Raman spectroscopic profiles, X-ray diffractograms, and SEM-EDAX patterns were acquired to examine pre- and post-treatment features of PANI and PANI-TiO_2 composites in the presence of RfOM.

Results and Discussion

FTIR-ATR Spectroscopy Analysis

The interactions between PANI and TiO_2 in PANI-TiO_2 composites were examined by FTIR-ATR spectroscopy and the stacked spectra were illustrated in Fig. 1.

The spectrum of bare PANI mainly included the characteristic peaks at 1584 cm^{-1} and 1481 cm^{-1} corresponding to C=N and C=C stretching vibrations of quinoid and benzenoid rings, respectively. The other benzenoid ring peaks at 1296 cm^{-1} and 1242 cm^{-1} were related to C–N stretching vibrations, while the peak at 797 cm^{-1} was attributed to C–C and C–H vibrations (Deng et al. 2016; Gu et al. 2012a). The peak at 1110 cm^{-1} was assigned to a quinoid ring of PANI, whereas the C-H out of plane bending vibration was located at 506 cm^{-1} (Pawar et al. 2010). The presence of surface anions in the protonated part of PANI was indicated by the peak at 579 cm^{-1} (Pawar et al. 2011). A wide peak centered at about 3366 cm^{-1} and a medium peak at 1639 cm^{-1} (Supplementary Material (SM), Part I, Fig SM.1) were noted in
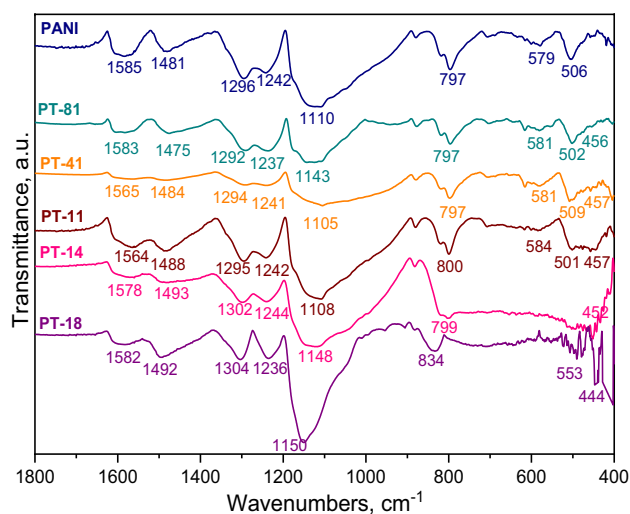

Fig. 1 FTIR-ATR spectra of PANI and PANI-TiO_2 composites

the spectrum of bare TiO_2 and associated with the stretching and bending vibration of OH groups on TiO_2 surface (Yalçın et al. 2010). The Ti–O bending mode was evident at 444–457 cm^{-1} (Yang et al. 2017). FTIR-ATR spectral features of PANI-TiO_2 composites revealed the appearance of peaks at 1584 cm^{-1}, 1481 cm^{-1}, 1296 cm^{-1}, 1242 cm^{-1}, 1110 cm^{-1}, 797 cm^{-1}, and 579 cm^{-1} confirming the presence of PANI in the composites (Fig. 1). The incorporation of TiO_2 in PANI-TiO_2 composites resulted in a gradual shift of typical PANI peaks of C=N (1584 cm^{-1}), C=C (1481 cm^{-1}), and C–N (1296 cm^{-1}). The tendency of titanium as a transition metal to form a coordination compound with nitrogen atoms of PANI could be attributed to the weakening of these bands to a lower wavelength of the peak at 1584 cm^{-1} corresponding to C=N stretching (Gilja et al. 2017). Beyond this threshold value, as the ratio of PANI increases, these bands gradually converged back to their initial wavenumber positions. The reason could be explained by the steep dilution of Ti–N interactions in the presence of very high PANI content up to PT-81 composite. The peaks related to TiO_2 were observed at wavenumbers lower than 900 cm^{-1} in composites for the represented wavelength interval.

FTIR-ATR spectra of PANI and PANI-TiO_2 specimens prior to and following photocatalytic degradation of RfOM were also presented in Fig. 2 and the related spectral peak assignments were listed in SM, Part I, Table SM1. Comparison of FTIR-ATR spectral variations due to adsorptive interactions or via non-selective oxidation revealed that the main peaks were evident under all conditions (Fig. 2a and b).

FTIR-ATR spectral features of RfOM were documented in detail as reported in our previous study (Uyguner-Demirel et al. 2022). FTIR-ATR spectra of RfOM were elucidated by various regions of functional groups and the first region of 3450–3200 cm^{-1} was associated with O–H stretching (alcohols, phenols, and carboxylic groups), N–H stretching (trace), and hydrogen-bonded OH. The wavenumber region as 3080–3030 cm^{-1} corresponded to aromatic C–H stretching, 2950–2840 cm^{-1} region was related to aliphatic C–H stretching (CH_3 and CH_2), and the peak in the region of 1660–1630 cm^{-1} belonged to C=O stretching of amide groups (amide I peak), C=O of quinone and/or H–bonded conjugated ketones. The peak at ~1575 cm^{-1} was related to COO^- in carboxylic acid salts (antisymmetric stretching). In the fingerprint region of RfOM, the band at ~1375 cm^{-1} was attributed to C–H bend (CH_3). The characteristic peaks in the fingerprint region between 1260–1200 cm^{-1} were ascribed as C–O stretching and OH deformation of COOH, C–O stretching of aryl ethers, and phenols present in RfOM structure. The other RfOM peaks in the fingerprint region were related to the C–O stretching of alcohols/aliphatic ethers (1095–1030 cm^{-1}) and out-of-plane bending of aromatic C–H, tri- and tetra substituted aromatic rings (975–775 cm^{-1}).
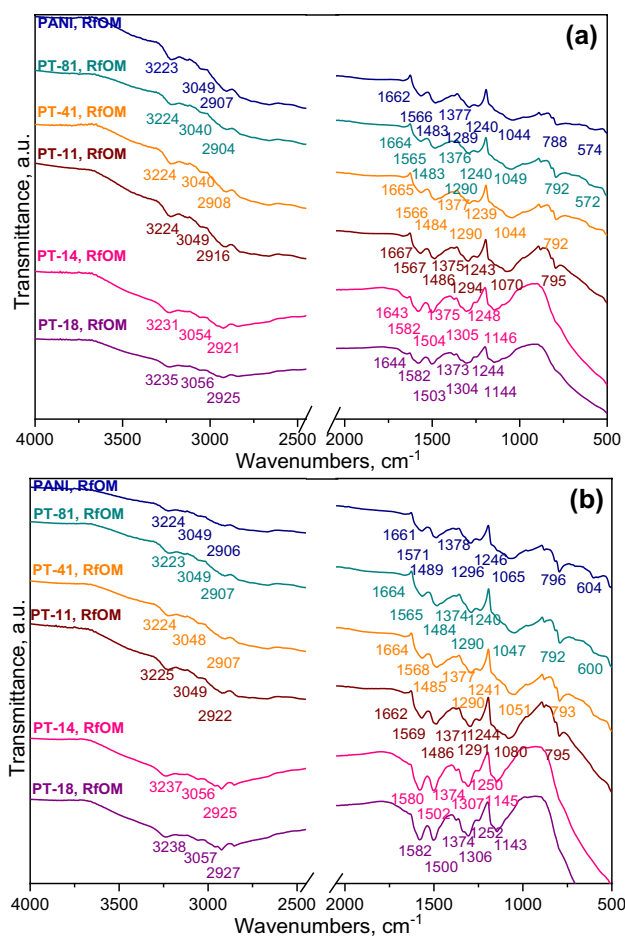

Fig. 2 FTIR-ATR spectra of RfOM on PANI and PANI-TiO_2 composites, (**a**) initial adsorption, (**b**) post-photocatalysis

The PANI and RfOM spectra displayed that the peak at 3223 cm^{-1} could be assigned to the associated O–H stretching (alcohols, phenols and carboxylic groups), N–H stretching (trace), and hydrogen-bonded OH of RfOM (Fig. 2 a). The peaks at 3049 cm^{-1} and 2907 cm^{-1} were related to aromatic C–H stretching and aliphatic C–H stretching of RfOM. The peaks at 1662 cm^{-1} (C=O stretching), 1377 cm^{-1} (C–H bending), 1240 cm^{-1} (C–OH stretching), and 1044 cm^{-1} (C–O stretching) appeared as an indication of RfOM adsorbed on the surface (Rodríguez et al. 2016; Senesi et al. 2003). Slight shifts of the bare PANI peaks were also evident due to adsorption of RfOM. PANI and RfOM peaks were likely to overlap and contribute together to several peaks. The peak located at 1566 cm^{-1} could be COO^- in carboxylic moieties of RfOM or C=N stretching in quinoid rings of PANI. Besides, the peak at 1240 cm^{-1} could be assigned to both C–O stretching peak of RfOM and C–N stretching of benzenoid unit of PANI. The peak at 788 cm^{-1} was related to out-of-plane bending of aromatic C–H peak of RfOM or C–C and C–H vibrations of PANI. Similar FTIR-ATR spectral features of PANI and

RfOM were reported by Zhang and colleagues (Li et al. 2011; Zhang et al. 2010). Compared to the spectra of PANI and RfOM, the peaks at 3223 cm^{-1}, 3049 cm^{-1}, and 2907 cm^{-1} shifted to higher wavenumbers with increasing TiO$_2$ content, especially in the spectra of PT-14 and "PT-18 and RfOM". The peaks at ~1570 cm^{-1} (νCOO$^-$ of RfOM or νC=N of PANI), ~1240 cm^{-1} (νC–O of RfOM or νC–N), ~790 cm^{-1} (δC–H of RfOM or νC–C and C–H of PANI) could be referred to the presence of either RfOM or PANI (Deng et al. 2016; Gu et al. 2012a; Rodríguez et al. 2016; Senesi et al. 2003). Slight shifts were recorded in all specimens except PT-14 and PT-18. The shift of peak from 1289 cm^{-1} (PANI) to ~1305 cm^{-1} (PT-14 and PT-18) most probably could be due to the varying amount of TiO$_2$ in the composite indicating the interaction between nitrogen atoms of PANI and oxygen atoms of TiO$_2$. Moreover, the electron transfers pertaining between PANI and TiO$_2$ resulted in the shift of peaks to higher wavenumbers (Sarmah and Kumar 2011). With increasing TiO$_2$ concentration, the peak at 575 cm^{-1} related to the surface anions of the protonated part of PANI vanished. Besides, the peak at ~1640 cm^{-1} could possibly indicate the stretching and bending vibration of OH groups on TiO$_2$ surface or C=O stretching of RfOM.

Following irradiation of RfOM in the presence of bare PANI, the changes observed for the functional groups were almost identical expressing the presence of the characteristic peaks originating from both counterparts (Fig. 2b). However, a significant shift was detected for the peak at 574 cm^{-1} to a higher wavenumber as 604 cm^{-1}. An increase in peak intensity indicating the presence of surface anions in the protonated part of PANI was also noticed. The reason could be explained by the dissociation of anions during the photocatalytic process. The presence of PANI peaks following irradiation designated that the molecular structure of PANI was not affected during treatment indicating stability under photocatalytic conditions. In PANI-TiO$_2$ composites and RfOM spectra, no significant difference between pre- (initial adsorption) and post-photocatalytic conditions was observed (Fig. 2b). All specimens exhibited slight shifts and similar trends with respect to the high molar ratio of TiO$_2$. Interestingly, only the peak assigned to surface anions was shifted to 600 cm^{-1} the reason of which could be associated with the change of surface anions in the protonated part of PANI upon photocatalysis.

Raman Spectroscopy Analysis

Raman spectra of PANI, TiO$_2$, and PANI-TiO$_2$ composites were presented in Fig. 3a-c. Raman spectrum of bare PANI displayed wide bands centered at 1567 cm^{-1} and 1345 cm^{-1} that were assigned to C=C stretching of the quinoid unit and C–N$^{+\bullet}$ stretching vibration, respectively (Fig. 3a) (Tao et al. 2007). Raman spectrum of TiO$_2$ revealed five characteristic anatase bands at 630 cm^{-1} (E$_g$), 508 cm^{-1} (A$_{1g}$), 388 cm^{-1} (B$_{1g}$), 188 cm^{-1} (E$_g$), and 134 cm^{-1} (E$_g$) (Ohsaka et al. 1978). Raman spectra of PANI-TiO$_2$ composites confirmed the coexistence of PANI and TiO$_2$ counterparts (Fig. 3b). The TiO$_2$ anatase band at 508 cm^{-1} which was only observed for PT-18 and PT-14 composites, disappeared with the increase of PANI ratio in the composites. The reason could be related to the high content of PANI, that decreased the polarizability of TiO$_2$ (Wang et al. 2017). Furthermore, due to the development of strong π-π interactions between PANI and TiO$_2$, the main band of TiO$_2$ at 134 cm^{-1} shifted to the higher absorption bands of the composites (Jeong et al. 2014). The C=C stretching band apparently shifted from 1567 cm^{-1} to 1560 cm^{-1} and the intensities of these bands gradually diminished with the addition of TiO$_2$ (Fig. 3c). The band intensity decreased further with the increase in the amount of PANI in composites due to the low conductivity of PANI (Wang et al. 2017).

Raman spectra of PANI and PANI-TiO$_2$ specimens in the presence of RfOM were recorded in order to detect the possible structural changes prior to and following photocatalytic treatment (Fig. 4a and b). The related characteristic Raman band assignments for RfOM, PANI, and TiO$_2$ were listed in SM, Part II, Table SM2.

The vibrational assignment of RfOM was reported on the basis of literature information outlined by various research groups (Francioso et al. 1996; Sánchez-Cortés et al. 1998, 2006). The most prominent bands of RfOM obtained in the region of 1680–1600 cm^{-1} were attributed to the amide I (C=O, C–N, N–H), the region of 1675–1630 cm^{-1} to the amide II (N–H deformation in proteins, C–N, N–H), the region of 1590–1580 cm^{-1} to the COO$^-$ asymmetric stretching of carboxylic acid, aromatic C=C stretching, the region of 1495–1440 cm^{-1} to the C–H$_2$ deformation, C–H bending, the region of 1410–1400 cm^{-1} to the COO$^-$ symmetric stretching of carboxylic acids, and the region of 1290–1210 cm^{-1} to the C–O stretching in phenols/CH$_2$ deformation. The bands in the region of 990–950 cm^{-1} were ascribed to the aromatic C–H out-of-plane deformation or anions. The bands in the region of 920–845 cm^{-1} were attributed to O–O stretching while those in the region of 920–875 cm^{-1} could belong to C–O–C stretching. The other bands at around 660 cm^{-1} and 550 cm^{-1} were ascribed to C–S stretching and C–C twisting of proteins (tyrosine) and C–C out of plane deformation, respectively. The bands in the region of 500–400 cm^{-1} could be assigned to C=O out of plane deformation carbohydrates. It should also be indicated that the specified organic groups constituted the main structural units of RfOM.

The Raman spectra of adsorbed RfOM on PANI and PANI-TiO$_2$ composites were presented in Fig. 4a. The spectra of PANI and RfOM exhibited the characteristic bands of both PANI and RfOM originating from the adsorption of PANI
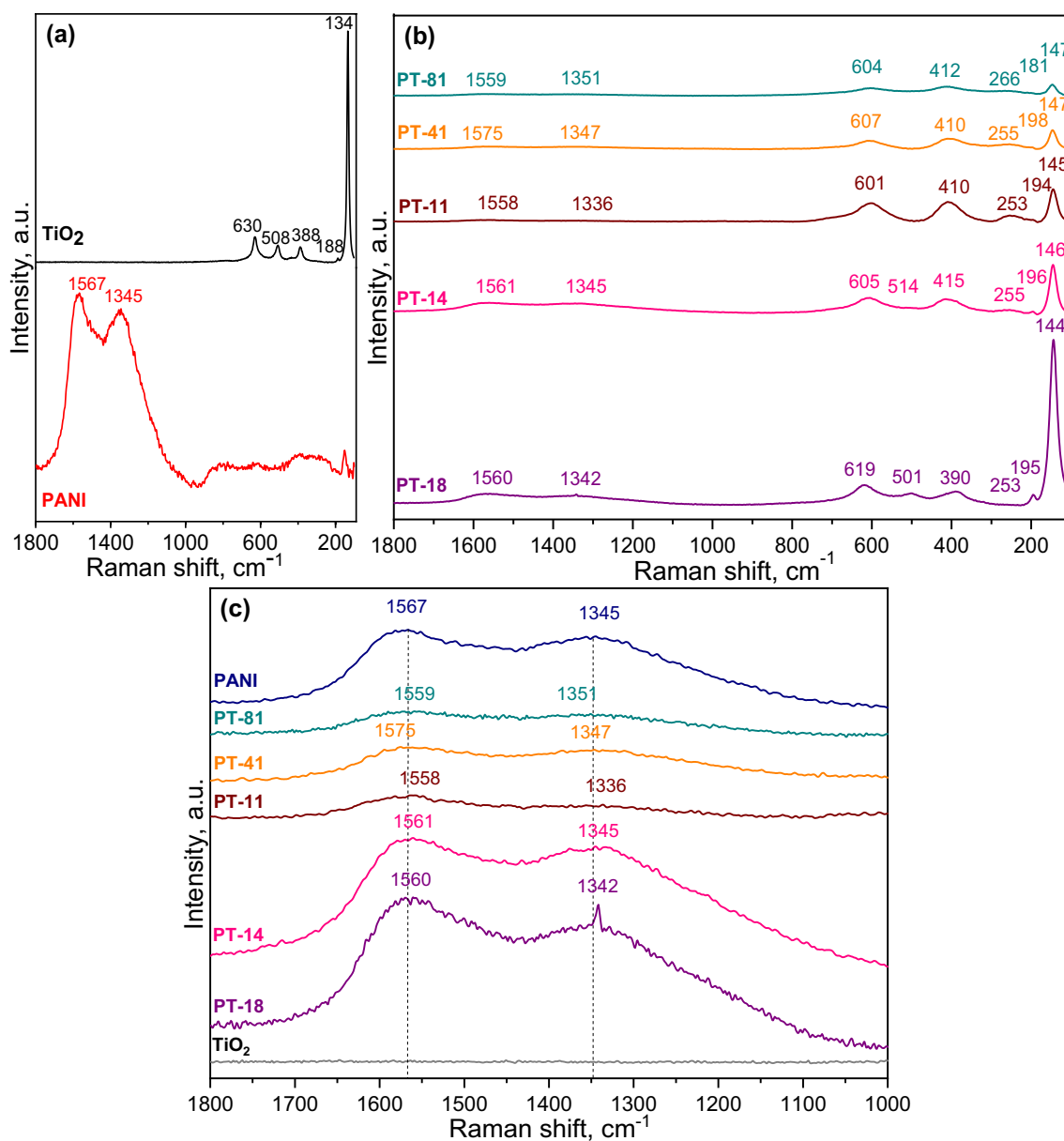
Fig. 3 Raman spectra of (**a**) PANI and TiO$_2$, (**b**) PANI-TiO$_2$ composites, (**c**) PANI, TiO$_2$, and PANI-TiO$_2$ composites (enlarged)

and RfOM onto TiO$_2$ surface. The wide main bands of bare PANI located at 1567 cm^{-1} and 1345 cm^{-1} corresponded to C=C stretching of the quinoid unit and C–N$^{+\bullet}$ stretching vibration, respectively (Fig. 3) (Tao et al. 2007). Compared to bare PANI, these two bands were blue-shifted to 1554 cm^{-1} and 1369 cm^{-1} due to adsorption of humic moieties on PANI and signified the bonding interactions between PANI and RfOM. The bands related to C=C stretching and C–N$^{+\bullet}$ stretching vibrations of PANI were observed in PANI, RfOM and all PANI-TiO$_2$ composites. A slight shift was noted in the spectra of PANI-TiO$_2$ composites compared to the spectrum of PANI and RfOM. These shifts were attributed to the presence of TiO$_2$ in TiO$_2$-PANI composites.

RfOM features displayed comparatively higher intensity values in PT-11 spectra in comparison to PT-81 and PT-41 where the interaction with PANI-TiO$_2$ composites was much stronger. The reason could be explained by the strong interaction prevailing between the composites and RfOM. The observed band at around 605 cm^{-1} could be related to TiO$_2$ anatase (E$_g$) band present in PANI-TiO$_2$ composites (Ohsaka et al. 1978). Insignificant variations were detected in Raman spectral features of PANI and RfOM under both initial adsorption and post-photocatalytic conditions. The effect of variations of PANI ratio in composites could not be visualized in their respective Raman spectral features (Fig. 4a and b). Moreover, the persistence of characteristic bands

Fig. 4 The Raman spectra of RfOM on PANI and PANI-TiO$_2$ composites, (**a**) initial adsorption, (**b**) post-photocatalysis
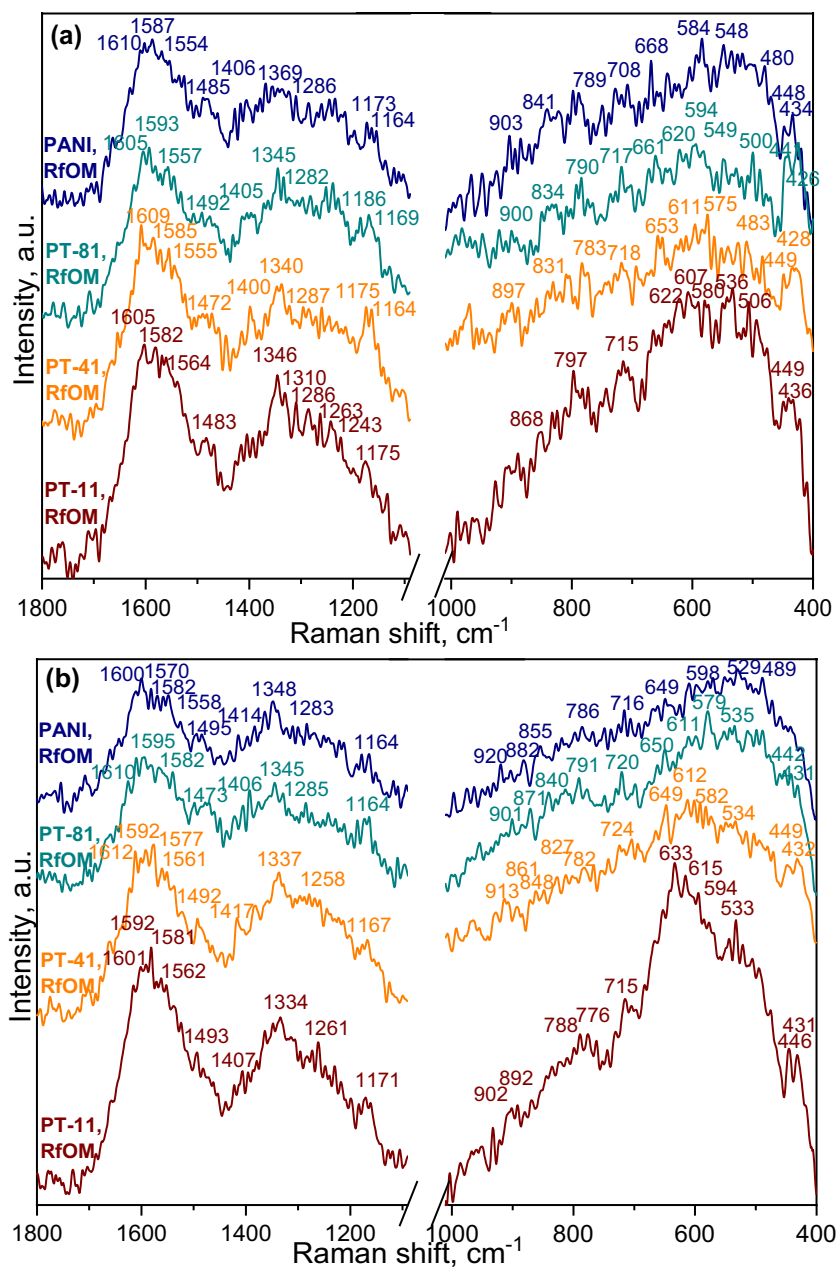
upon exposure to irradiation demonstrated the photocatalytic stability of PANI.

XRD Analysis

The broad XRD peaks related to zones at $2\theta = 8.99°$, $15.42°$, $20.34°$, $25.30°$, and $27.18°$ were ascribed to (0 0 1), (0 1 1), (0 2 0), (2 0 0), and (1 2 1) reflection planes respectively and expressed the semi-crystalline nature of PANI (Fig. 5 a) (Stejskal et al. 1998). The observed amorphous phase was related to the characteristic property of polymeric materials. The semi-crystalline feature was linked to the planar structure of benzenoid and quinoid rings that extended in

both horizontal and perpendicular directions with repetition. The peaks at $2\theta = 15.42°$ and $25.30°$ could be attributed to the parallel and perpendicular periodicity associated with the inter-planar spacing caused by polymer chains at $2\theta = 20.34°$. The presence of these bands indicated the emeraldine salt (conducting) form of PANI (Pal et al. 2020; Tang et al. 2008). The crystallite phases of TiO$_2$ were presented by anatase (JCPDS No. 73–1764) and rutile (JCPDS No. 99–0090) crystal structures. A series of characteristic peaks at $2\theta = 25.36°$, $37.08°$, $37.89°$, $38.69°$, $48.08°$, $53.98°$, $55.12°$, $62.82°$, $69.09°$, $70.38°$, $75.18°$, $76.19°$ were assigned to (1 0 1), (1 0 3), (0 0 4), (1 1 2), (2 0 0), (1 0 5), (2 1 1), (0 0 2), (1 1 6), (2 2 0), (2 1 5), and (3 0 1) planes of anatase,
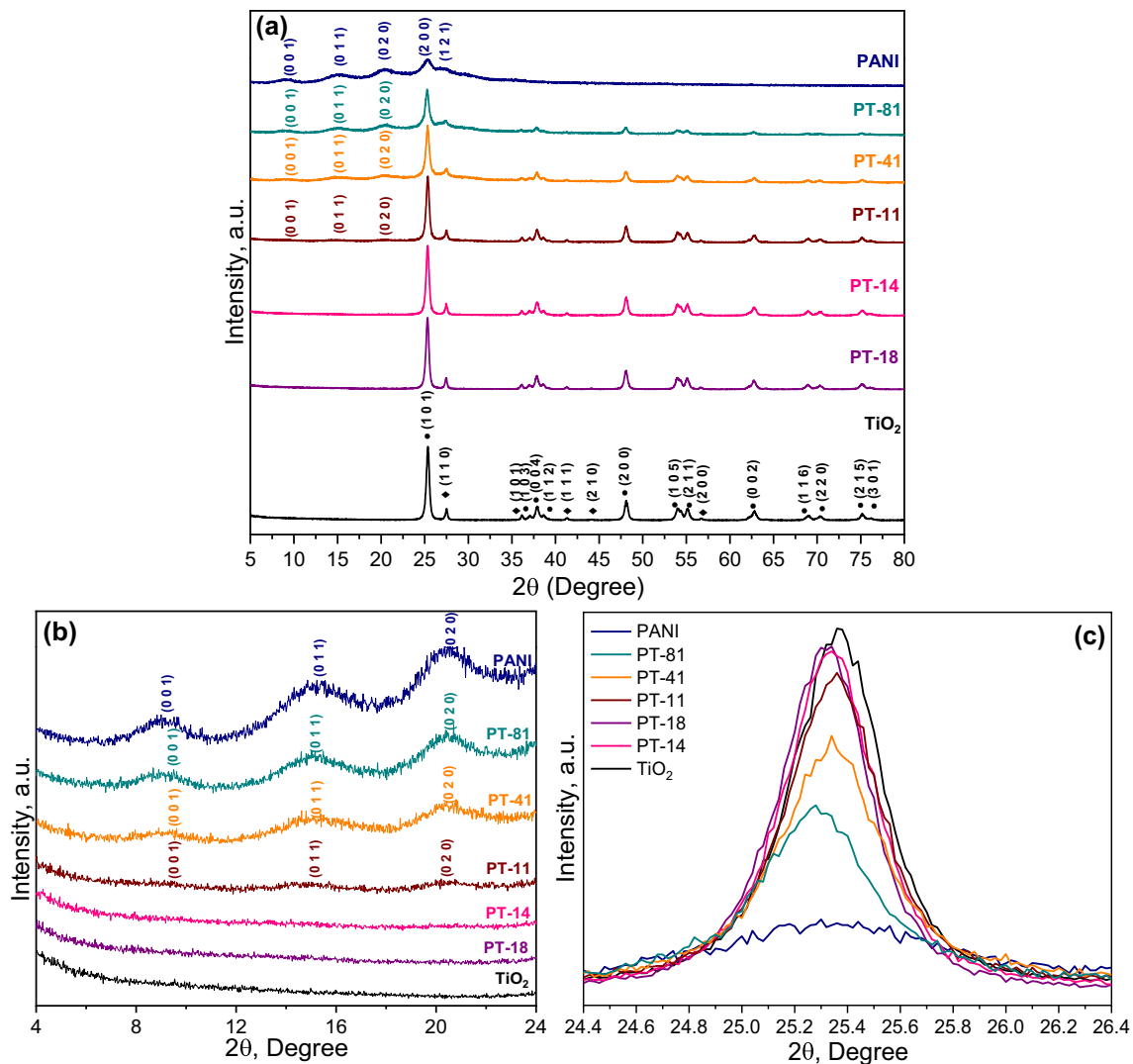
Fig. 5 (**a**) XRD diffractograms, (**b**) enlarged XRD diffractogram view, and (**c**) XRD peaks for (1 0 1) planes of PANI, TiO$_2$, and PANI-TiO$_2$ composites (● anatase, ◆ rutile)

while peaks at $2\theta = 27.52°$, $36.14°$, $41.34°$, $44.10°$, $56.74°$ corresponded to (1 1 0), (1 0 1), (1 1 1), (2 1 0), and (2 0 0) planes of rutile, respectively.

In XRD patterns of PT-81, PT-41, and PT-11 (Fig. 5b), three peaks of PANI at $8.99°$, $14.86°$, and $20.34°$ clearly appeared, while the peak at $25.30°$ was found to be shielded by (1 0 1) anatase plane of TiO$_2$. In these composites with increasing PANI content, the crystalline character of TiO$_2$ slowly decreased and the amorphous character of PANI increased due to the strong interactions between PANI and TiO$_2$ giving rise to the deposition of PANI on the surface of TiO$_2$ rather than packing of polyaniline chains to form a semi-crystalline structure (Monfared and Jamshidi 2019). This trend was monitored especially in PT-81 and PT-41 composites with the two highest PANI ratios and a completely amorphous PANI surface was observed for the other

composites as the TiO$_2$ ratio increased. Besides, it should be noted that the peak positions and widths of the composites containing higher PANI ratios clearly differed from TiO$_2$ indicating that the lattice structure was influenced by the modification process. The widening and shifting to a lower position of diffraction peaks related to the dominant lattice plane of (1 0 1) were demonstrated in Fig. 5c and the results were given in SM, Part III, Table SM3. A slight alteration in peak positions was observed in composites with decreasing PANI ratios, indicating that PANI acted as a modifier and that these composites could be more favorable to photocatalysis. In comparison to bare TiO$_2$, almost no significant change was traced in the phase ratio of PANI-TiO$_2$ composites.

The most prominent peak of (1 0 1) was usually chosen to calculate the crystallite size of PANI-TiO$_2$ composites by

Fig. 6 SEM micrographs (left)×100000, (right)×50000 of (**a**) PANI, (**b**) PT-81, (**c**) PT-41, (**d**) PT-11, (**e**) PT-14, (**f**) PT-18, (**g**) TiO$_2$
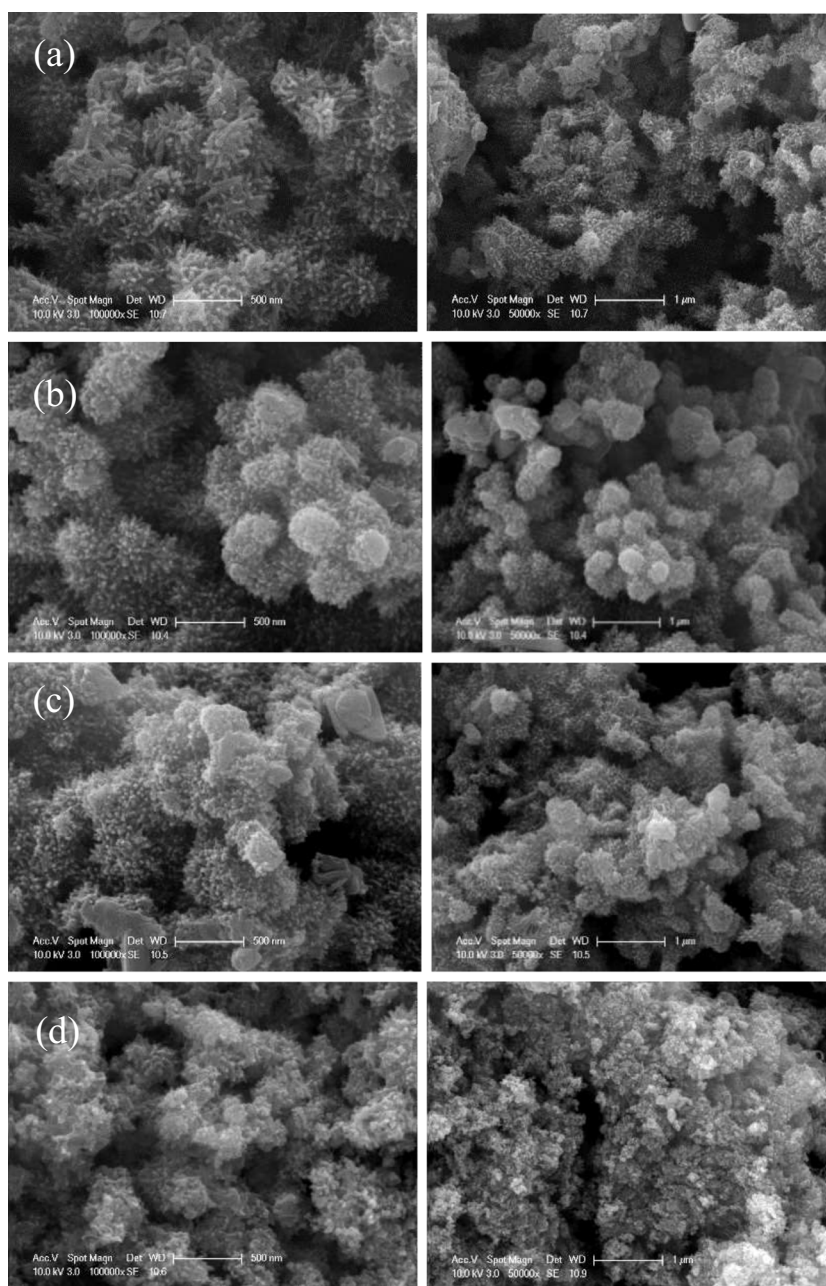

using Sherrer's equation (Eq. 1) (Liao et al. 2011; Rahman and Kar 2020b). However, this characteristic anatase plane overlapped with the (2 0 0) plane of PANI, which might be misleading. Therefore, the relatively intense anatase (2 0 0) plane was also chosen to compare the crystallite sizes of TiO$_2$ and PANI-TiO$_2$ composites. The crystallite sizes of TiO$_2$ and PANI-TiO$_2$ composites corresponding to the (1 0 1) plane were in the range of ~17–20 nm. The crystallite size of bare PANI at this plane was calculated as ~11 nm. PANI modification exerted an insignificant effect on the lattice structure of TiO$_2$ as inferred from the calculated crystallite sizes (~20 nm) corresponding to (2 0 0) plane. The XRD diffractograms of PANI and representative PANI-TiO$_2$ composites in the presence of RfOM under post- photocatalytic conditions were presented in SM, Part III, Fig SM.2.

It was reported that RfOM revealed an amorphous nature containing two weak peaks at $2\theta = 28.61^\circ$ and 45.40° (Preethika and Sundramoorthy 2019). The two main diffraction peaks of PANI were observed at $2\theta = 15.42^\circ$ and 25.30° shifted to $2\theta = 13.46^\circ$ and 25.52° respectively in the presence of RfOM and upon irradiation (SM, Part III, Fig SM.2). The peaks at $2\theta = 25.28^\circ$ and 25.36° in PT-81 and PT-11 diffractograms slightly shifted towards higher angle positions (25.46° and 25.42°) in the presence of RfOM indicating no significant change so that the crystalline structure of the composites was maintained.

Fig. 6 (continued)
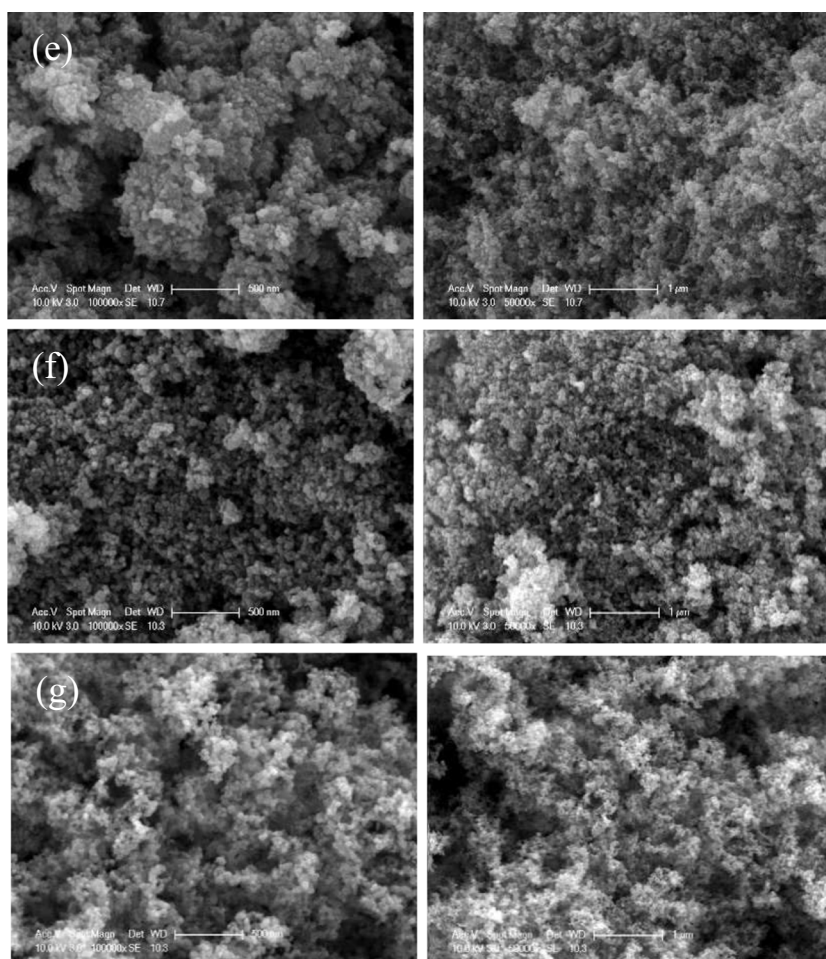
The lattice constants for TiO$_2$ and PANI-TiO$_2$ composites were determined by using the XRD peaks of anatase (1 0 1) and (2 0 0) planes. The respective lattice parameters were presented in SM, Part III, Table SM3. The lattice constants for TiO$_2$ were calculated as $a=b=3.7847$ Å, $c=9.4232$ Å, and the values were found as; $a=b=3.7847$ Å, $c=9.4778$ Å for PT-18. This negligible increase in "c" indicated that TiO$_2$ stretching occurred along c-axis and was suppressed along the horizontal direction. A slight change was observed in the lattice constants "a" and "c" with increasing PANI amounts in PANI-TiO$_2$ composites up to PT-81. However, the presence of a high amount of PANI in composite (PT-81) led to a slightly higher increase in the lattice constants and cell unit volume that could be attributed to the overlapping planes of anatase (1 0 1) TiO$_2$ and PANI. This overlapping was also seen in the enlarged XRD diffractograms of PANI and PT-81 as presented in Fig. 5c. The minor moderation in lattice parameters implied a slight stretching of the unit cell. The reason could be the addition of PANI which results in an interaction such as the adsorption of PANI chains on the surface of TiO$_2$ particles.

SEM-EDAX Analysis

SEM micrographs of PANI, TiO$_2$, PANI-TiO$_2$ composites were presented in Fig. 6a-g, and corresponding EDAX spectral features were given in SM, Part IV, Fig SM.3–5. The surface morphology of PANI consisted of slightly aggregated particles in a relatively homogeneous distribution resembling a dandelion like shape. SEM image of TiO$_2$ consisted of tiny and almost spherical TiO$_2$ particles. PT-18 composite exhibited a rather uniform and similar morphology to TiO$_2$ most probably due to lower content of PANI. Contrary to the slight agglomeration of TiO$_2$ in PT-18, a more aggregated morphology was evidenced for PT-14 composite. The particle/agglomerate size of PT-14 (Fig. 6e) was slightly larger than that of bare TiO$_2$ (Fig. 6g) due to the presence of PANI on the oxide surface. In the micrograph of PT-11 composite, an almost equal contribution of both small TiO$_2$ and large PANI particles was clearly observed. With a further increase in the ratio of PANI, a high agglomeration tendency was detected. SEM image of PT-81 displayed flower-like shapes of PANI particles with larger agglomerates as ∼300 nm due

**Fig. 7** SEM micrographs (left)×100000, (right)×50000 of (**a**) PANI, (**b**) PANI and RfOM, initial adsorption, (**c**) PT-81, (**d**) PT-81 and RfOM, initial adsorption, (**e**) PT-41, (**f**) PT-41 and RfOM, initial adsorption, (**g**) PT-11, (**h**) PT-11 and RfOM, initial adsorption
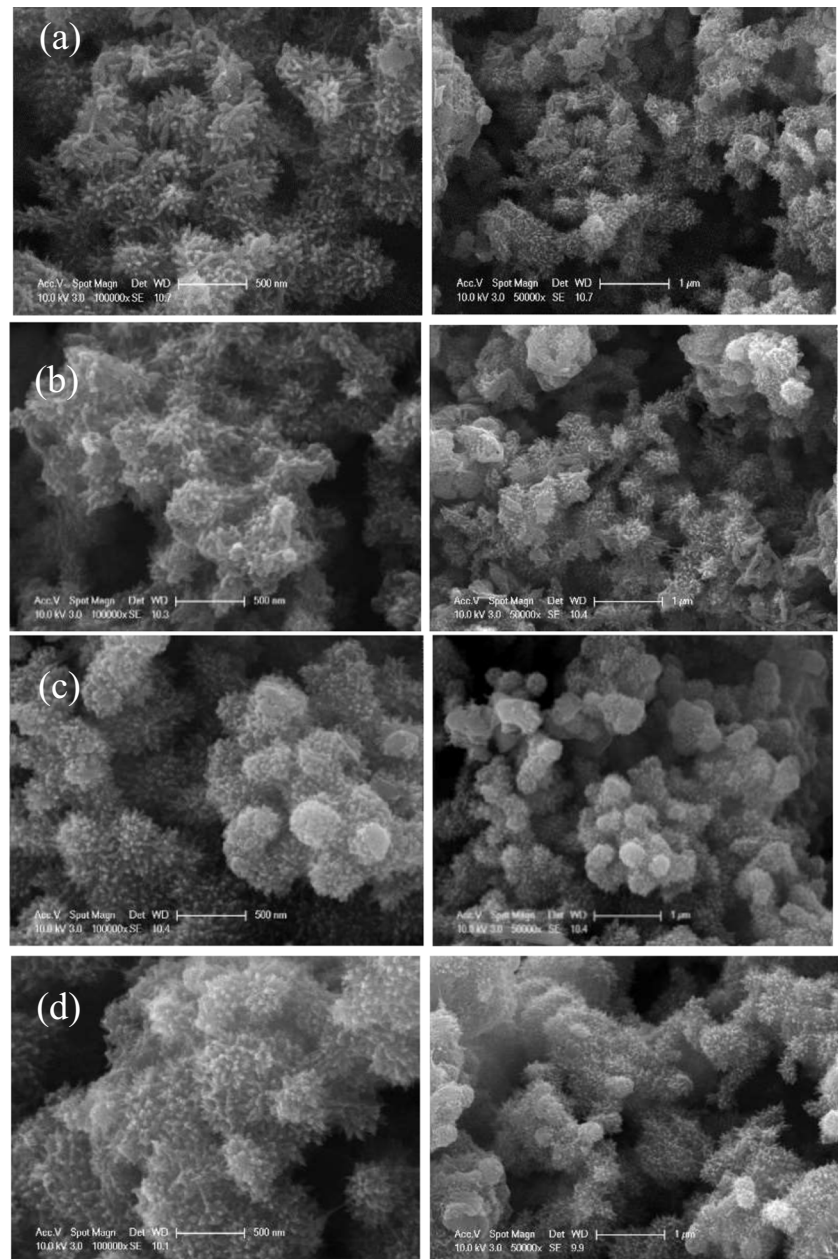
to the extensive surface coverage of TiO$_2$ with PANI. EDAX analysis showed that C, N, Cl, O, and Ti were present in PANI and PANI-TiO$_2$ composites as expected. It was evident that at high PANI ratios in PANI-TiO$_2$ composites, the amount of C in EDAX analysis also increased. SEM images could also be used to examine changes in the surface morphology of PANI and PANI-TiO$_2$ composites in the presence of RfOM before and following photocatalysis as presented in Figs. 7 and 8, respectively. The effect of PANI contribution to the composite structure was preferentially investigated for PT-81, PT-41, and PT-11 specimens composed of higher PANI ratios. For practical reasons and ease of comparison, SEM images of selected samples (Fig. 6) were also given in

Figs. 7 and 8 (PANI Fig. 6a was also given as Figs. 7a and 8a, PT-81 Fig. 6b as Fig. 7c and Fig. 8c, PT-41 Fig. 6c as Fig. 7e and Fig. 8e, PT-11 Fig. 6d as Fig. 7g and Fig. 8g). It could be observed that the dandelion like shape of bare PANI powder (Fig. 7a) was slightly deformed and individual components were partially combined resulting from RfOM adsorption (Fig. 7b). The resulting morphology following photocatalytic treatment revealed the formation of irregular structures via RfOM degradation (Fig. 8b). A comparison of SEM images of PT-81 composites before and after adsorption of RfOM pointed out a morphological change (Fig. 7c, d). A local agglomeration phenomenon was observed due to the inter-active forces prevailing between the dense PANI component

Fig. 7 (continued)
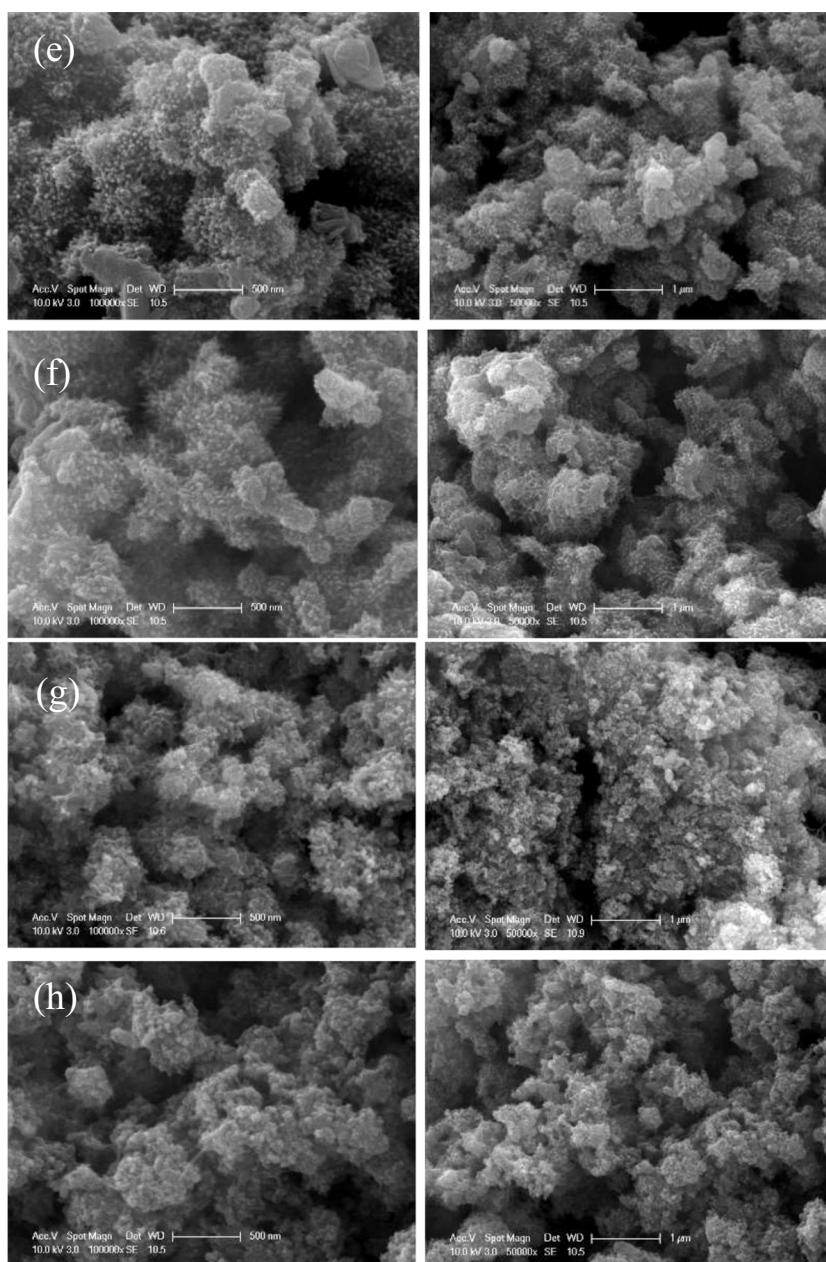
of PT-81 and RfOM. Following photocatalysis, the morphology of PANI in PT-81 composite was almost altered, and newly shaped structures with smoother surfaces were formed (Fig. 8d). Therefore, as to PT-81 composite, the extensively covered surface with RfOM could lead to inefficient performance during photocatalysis. The tendency of surface coverage with RfOM was also evident for PT-41 following initial adsorption compared to bare PT-41 devoid of organic matrix (Fig. 7e, f). The surface deformation was very similar to that of the PT-81 composite of (Fig. 8d) following photocatalytic treatment (Fig. 8f). A comparison of Fig. 7g and Fig. 7h of PT-11 revealed that the surface coverage of RfOM was weakened and a slight deformation was observed under initial adsorption conditions. The morphology of PT-11 was mostly maintained after photocatalytic treatment. A slight tendency of agglomeration and formation of larger sized particles was observed (Fig. 8h). The photocatalytic removal efficiencies of RfOM (UV_{254}) for PANI, PT-81, PT-41, and PT-11 specimens were reported as 81%, 62%, 69%, and 74%, respectively (Uyguner-Demirel et al. 2023). The excessive formation of aggregates could possibly exert a retardation effect on the removal efficiency of PT-81 compared to PT-41 and PT-11. It was noteworthy that the carbon content in EDAX spectra of all specimens decreased after photocatalytic treatment compared to the values obtained after adsorption due to the degradation of RfOM.

Fig. 8 SEM micrographs (left)×100,000, (right)×50,000 of (**a**) PANI, (**b**) PANI, and RfOM, post-photocatalysis, (**c**) PT-81, (**d**) PT-81 and RfOM, post-photocatalysis, (**e**) PT-41, (**f**) PT-41 and RfOM, post-photocatalysis, (**g**) PT-11, (**h**) PT-11 and RfOM, post-photocatalysis
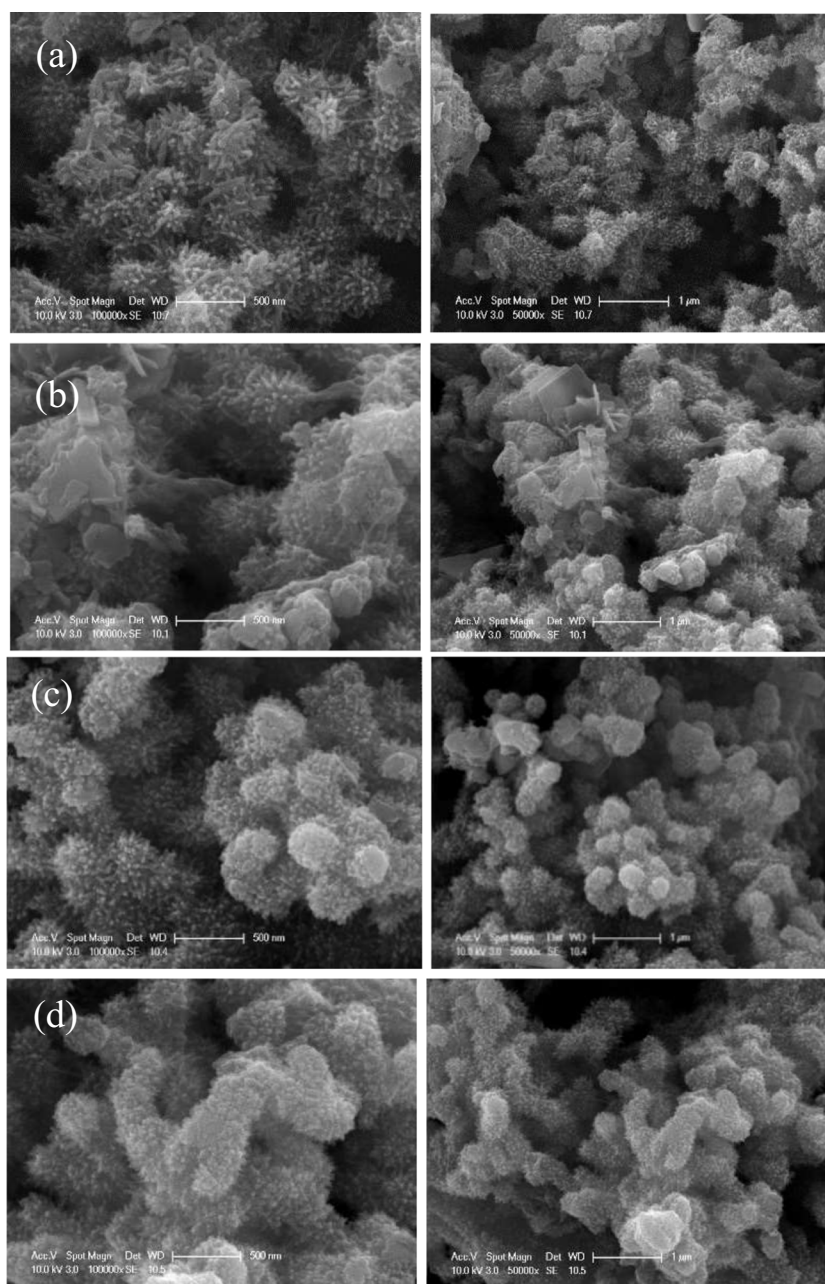

XPS Analysis

XPS analysis was performed to provide further evidence of the presence of PANI by assessing the elemental composition, oxidation state, and degree of protonation in PANI-TiO_2 composites. Moreover, these measurements could help in unraveling the surface modification of TiO_2 that was affected by the deposition of PANI. Comparative spectra of PANI, TiO_2, and PANI-TiO_2 composites were illustrated in Fig. 9a. The XPS survey scan of PANI exhibited four elements, namely C, N, O, and Cl while the spectra of PANI-TiO_2 composites contained Ti, O, C, N, and Cl. This confirmed the presence of PANI in PANI-TiO_2 composites. The

C1s peak located at 284.56 eV in the TiO_2 spectrum could be ascribed to the adventitious carbon that was applied to calibrate the scale of binding energy (Djaballah et al 2023). The spectroscopic parameters of deconvoluted peaks and their related orbitals were illustrated in SM, Part V, Table SM4.

The deconvoluted C1s spectra of PANI and PANI-TiO_2 composites were displayed in Fig. 9b-d. By analyzing the spectrum of PANI, C1s core shell demonstrated five peaks with binding energies at 283.61 eV, 284.21 eV, 284.87 eV, 285.64 eV, and 286.83 eV signifying the different forms of carbon present in PANI (Fig. 9b). The first peak at 283.61 eV in PANI was assigned to the presence

Fig. 8 (continued)
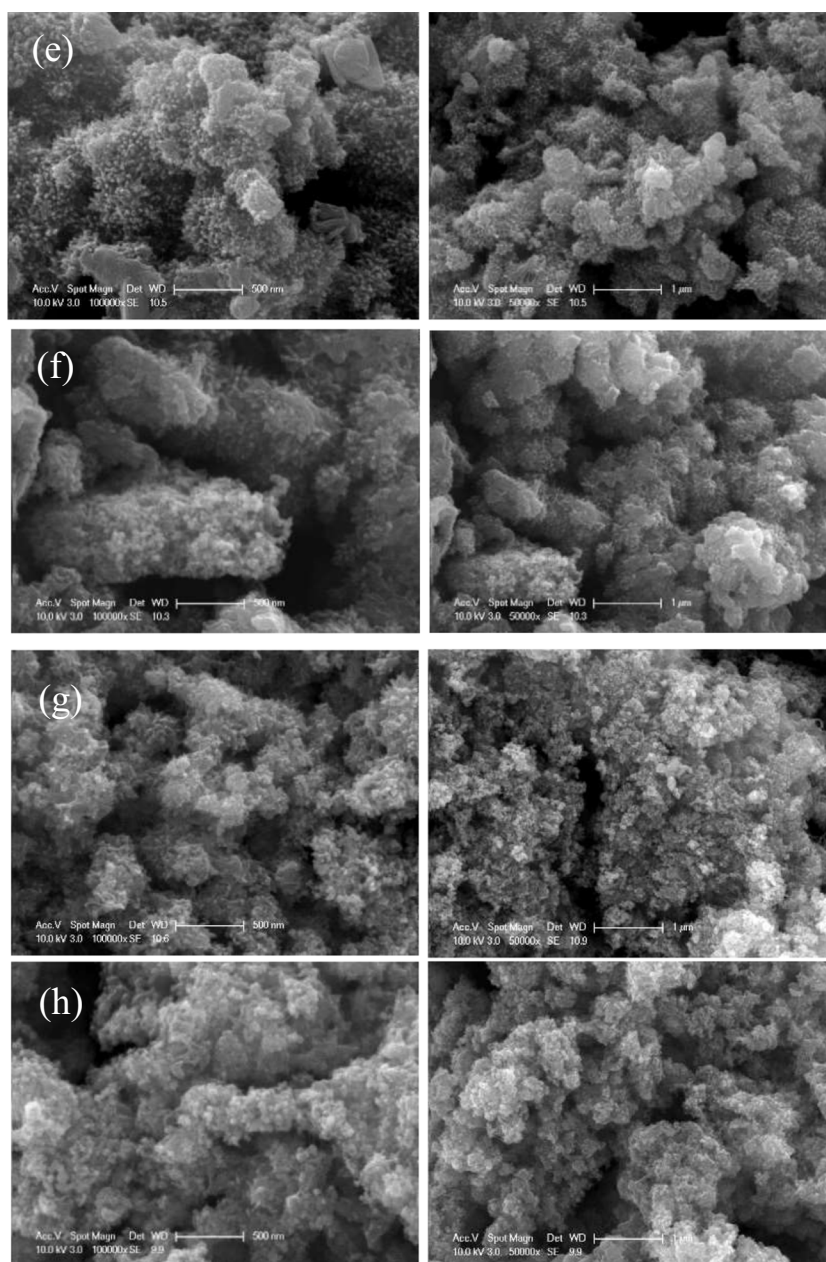
of aromatic C–H bond. The second peak at 284.21 eV corresponded to an aromatic C–C bond (Anirudhan et al. 2021; Kulkarni et al. 2019). The other C1s components at 284.87 eV and 285.64 eV were attributed to C = N or N–C, and C–N$^+$ or C = N$^+$ bonding, respectively. The small peak with high binding energy tailed at 286.83 eV could be assigned to the functional group C = O/C–O arising from the oxidation of PANI, as also explained in O1s spectra (Li et al. 2013). This was also an indication of the well doped states. The deconvoluted spectra of PT-41 composite revealed five main peaks at binding energy values of 283.44 eV, 283.99 eV, 284.63 eV, 285.39 eV, and 286.24 eV. These peaks shifted to lower binding energy

values as compared to bare PANI. Moreover, emergence of a new peak at 287.89 eV corresponding to Ti–O–N–C bonding was noticed (Gu et al. 2012a; Li et al. 2008a). The amount of TiO$_2$ increased several folds in PT-11 and PT-14 composites affecting the extent of Ti–O–N–C interaction (assigned at 288.69 eV and 288.40 eV, respectively). This finding could also be depicted from the relative areas of the corresponding binding peaks. Moreover, the satellite peak with high binding energy that could be attributed to the combination of probable protonation of imine and amine sites was observed for both PANI and PT-41, however disappeared in PT-11 and PT-14 specimens. The high level of Ti–O–N–C bonding could
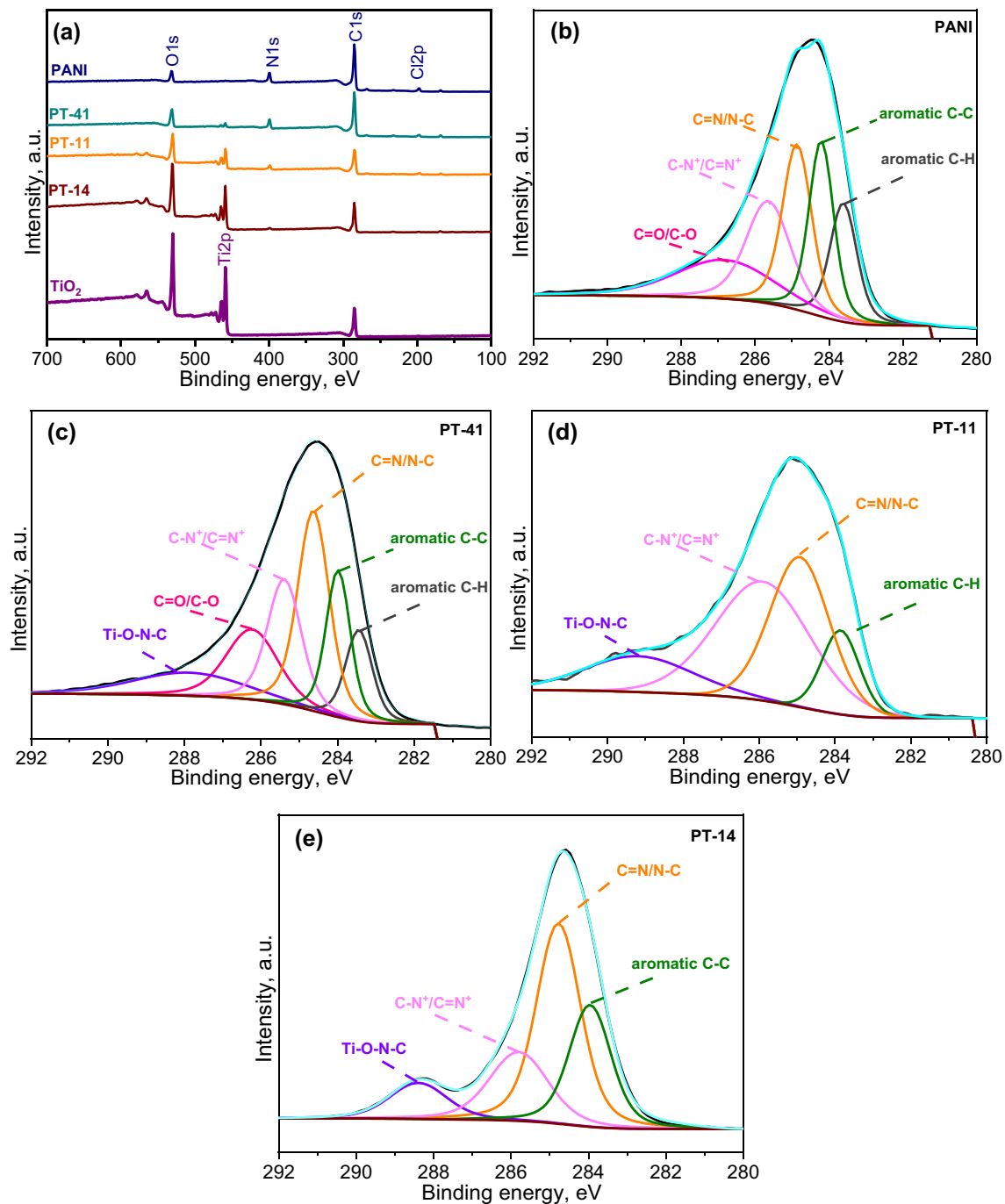
Fig. 9 XPS spectra of PANI, TiO$_2$ and PANI-TiO$_2$ composites (**a**) All survey spectra, (**b-e**) The C1s deconvoluted spectra

conceivably suppress the intramolecular interaction of PANI chains.

N1s core level spectra for PANI and all composites were given in Fig. 10a-e. The N1s spectrum of PANI was deconvoluted into three peaks (Fig. 10a). The major characteristic binding peak at 399.05 eV was attributed to undoped imine (–N=) and amine (–NH–) groups, whereas the peaks at 400.00 eV and 401.74 eV were assigned to positively charged

nitrogen present in protonated amine (–NH$^+$–) and protonated imine (–NH$^+$=) groups, respectively (Gu et al. 2012b; Singh et al. 2021).

The intrinsic oxidation state of PANI could be determined using quantitative parameters obtained from the XPS data. The percentages of area intensities for N1s were 50.02%, 37.35%, 12.62% for the peaks at 399.05 eV, 400.00 eV, and 401.74 eV, respectively. This result was consistent consistent
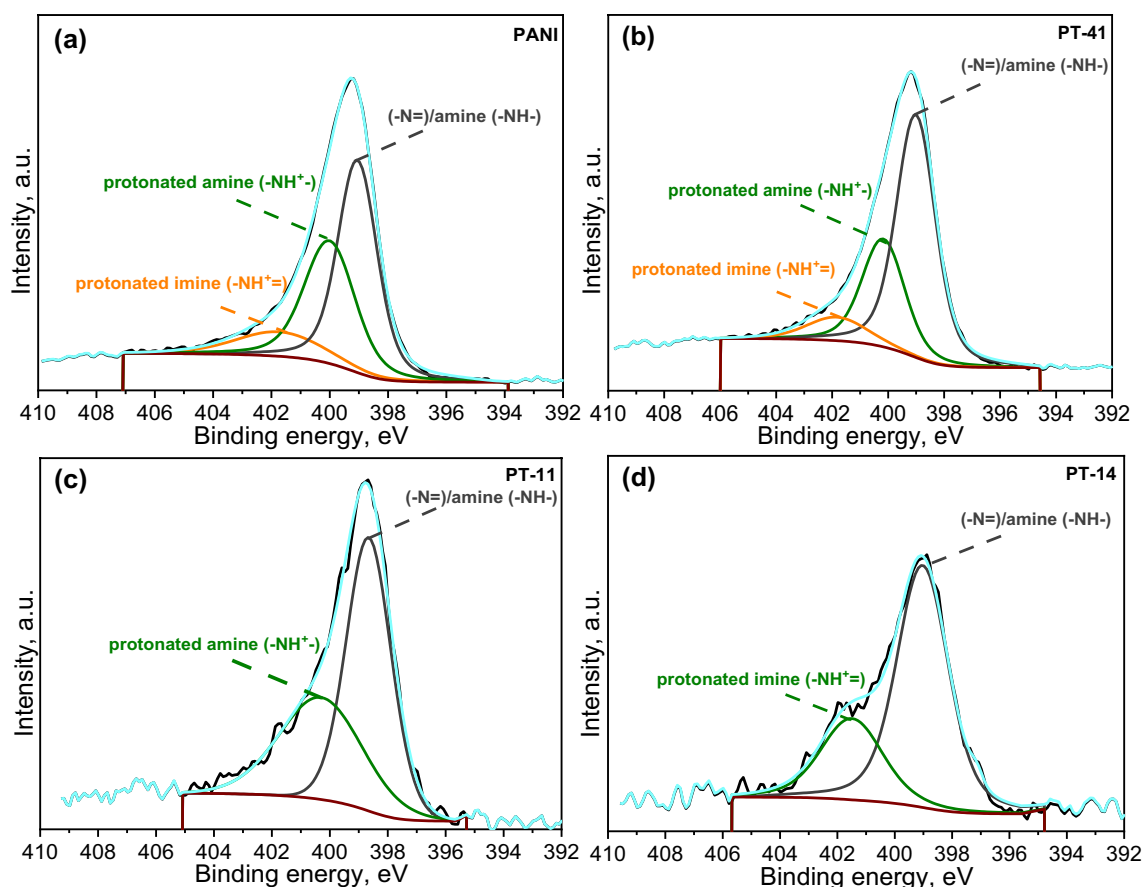
Fig. 10 The N1s deconvoluted XPS spectra of (**a**) PANI, (**b**) PT-41, (**c**) PT-11, (**d**) PT-14

with "amine/imine" ratio and the assumption that the intrinsic oxidation state of PANI was 50% oxidized emeraldine (y = ~0.5) with respect to the represented general formula of PANI as $[(–B–NH–B–NH–)_y(–B–N=Q=N–)_{1-y}]_x$ where B and Q were denoted as C_6H_4 rings in the benzenoid and quinoid forms, respectively (Gospodinova and Terlemezyan 1998; Golczak et al. 2008). PANI composition obtained from the XPS quantitative analyses revealed C (65.3%), N (12.3%), O (17.2%), and Cl (5.2%). The overall theoretical ratio of carbon to nitrogen in PANI derived from molecular formula $(C_6H_5N)_n$ was 6:1. However, total C/N ratio 5.32:1 was deduced that could be regarded as close to the theoretical value (Golczak et al. 2008; Kumar et al. 1990; Singh et al. 2021).

The deconvoluted N1s spectrum of PT-41 composite revealed three binding energies at 399.01 eV, 400.17 eV, and 401.83 eV that shifted to slightly higher binding energies compared to the ones observed for bare PANI (Fig. 10b). Although a red shift in these peaks for PANI composites with titania was also reported (Li et al. 2013), a blue shift was observed here as outlined for PANI composites with zinc titanate (Singh et al. 2021) and for polypyrrole composites with titania (Kang et al.

1998). The reason for this blue shift could be attributed to the interaction of nitrogen atoms with Ti^{4+} ions present in TiO_2 crystals. This was in accordance with the gradual shift of typical PANI peaks to higher wavenumbers with increasing PANI content as explained by FTIR-ATR spectral features. A similar trend was also observed for PT-11 and PT-14 composites, although the intensities of the signals were not as high as the other composites due to the comparatively low concentration of PANI. This was also a negative impact on the reliability of the deconvolution spectra of these composites (Fig. 10c, d).

Element analyses of Cl2p spectra in PANI and PANI-TiO_2 composites were shown in SM, Part V, Fig SM.6 a-d. The Cl2p core level spectrum of PANI was deconvoluted into four peaks at 196.75 eV, 197.35 eV, 198.32 eV, and 199.52 eV. The peaks at ~ 197 eV and ~ 199 eV were related to $2p_{3/2}$ (chloride anion) and $2p_{1/2}$ (covalently bound chlorine), respectively (Tan et al. 1989; Yue and Epstein 1991). The four peaks of Cl2p were observed in PT-41 composite, while the peaks at 197.13 eV and 200 eV related to $2p_{1/2}$ and $2p_{3/2}$, respectively, were located in the Cl2p spectrum of PT-14.
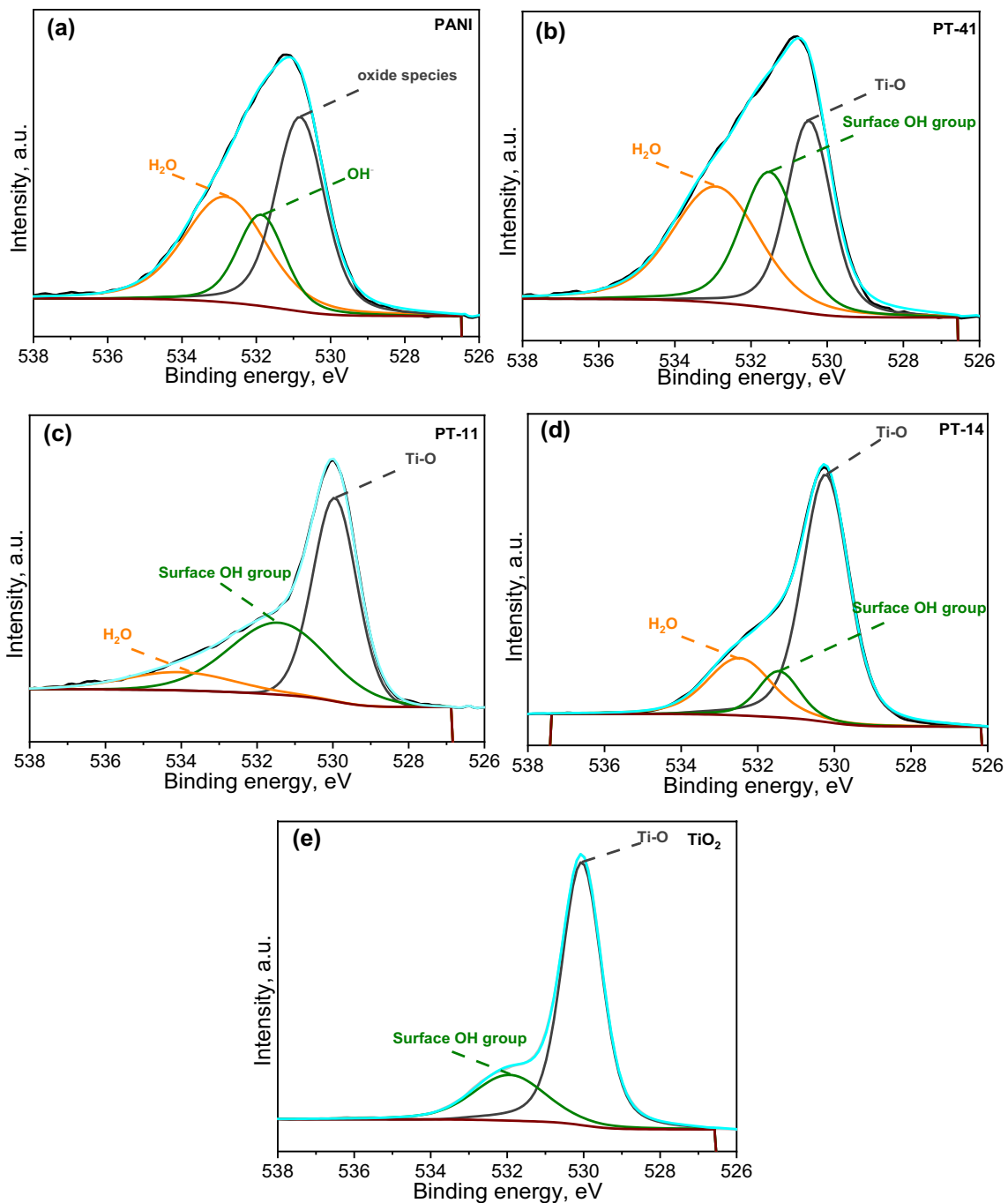
Fig. 11 The O1s deconvoluted XPS spectra of (**a**) PANI, (**b**) PT-41, (**c**) PT-11, (**d**) PT-14, (**e**) TiO_2

The O1s spectral region was employed for analyzing the oxygen states present in bare PANI, TiO_2, and PANI-TiO_2 composites, as shown in Fig. 11a-e. O1s spectrum of PANI displayed three forms of oxygen at 530.82 eV, 531.87 eV, and 532.84 eV. The lowest binding energy peak represented the C = O group, the peak at 531.87 eV was assigned to hydroxyl (C–OH) group-, and the peak at 532.84 eV corresponded to the adsorbed water (Golczak et al. 2008). The O1s core level spectrum of TiO_2 deconvoluted into two peaks at 530.05 eV and 531.94 eV which pointed out the typical Ti–O bond and surface OH bonds of TiO_2, respectively (Li et al. 2008b). In comparison to TiO_2, the binding energies of PANI-TiO_2 composites shifted to higher energy values due to the possible formation of hydrogen bonding between PANI and TiO_2 (TiO_2–O–HN–PANI) (Wang et al. 2017).
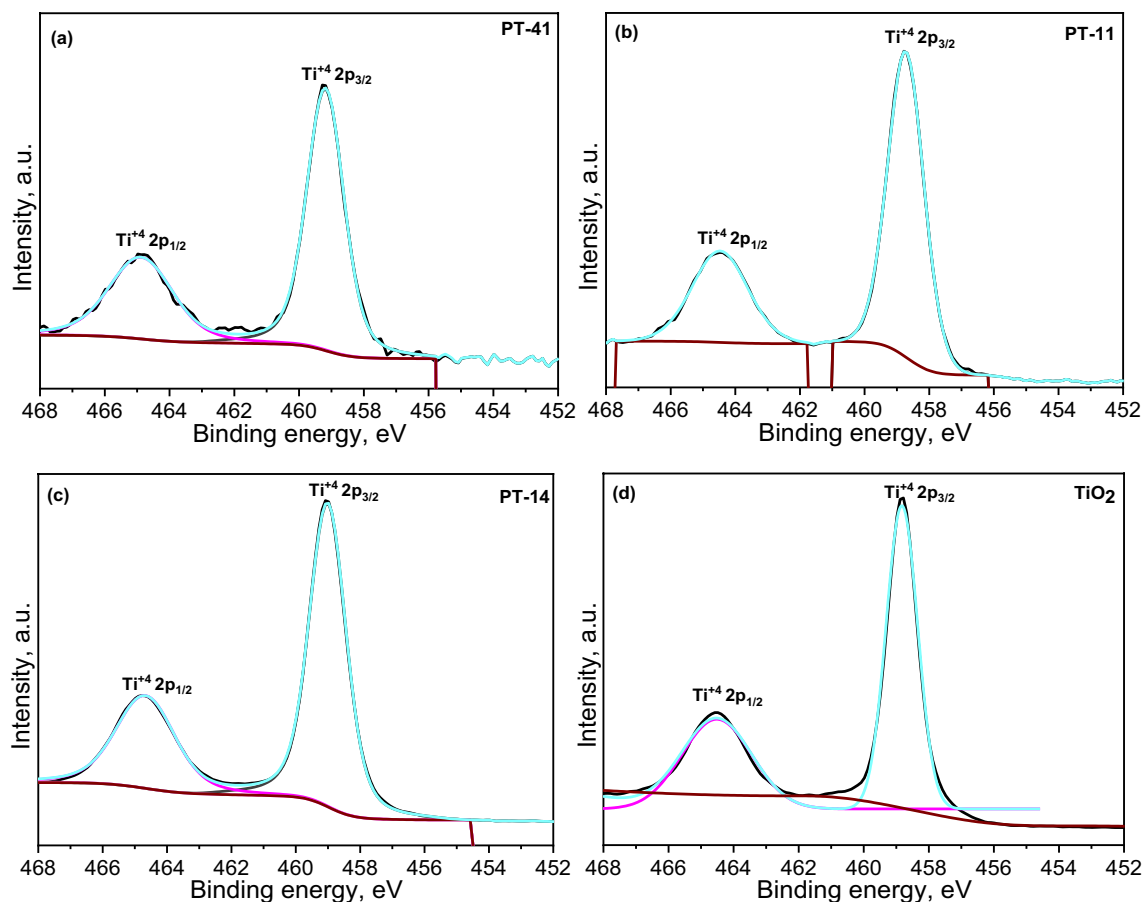
Fig. 12 The Ti2p deconvoluted spectra of (**a**) PT-41, (**b**) PT-11, (**c**) PT-14, (**d**) TiO$_2$

Moreover, Fig. 12a-d revealed XPS profiles related to Ti2p core level of TiO$_2$ and PANI-TiO$_2$ composites. The peaks at 458.78 eV and 464.48 eV were assigned to Ti^{+4} 2p$_{3/2}$ and Ti^{+4} 2p$_{1/2}$, respectively (Fig. 12d) (Bessergenev et al. 2015). In comparison to TiO$_2$, the binding energy of Ti2p in the composites shifted to higher values with increasing PANI content as expected. XPS data indicated strong interactions prevailing between PANI and TiO$_2$ most probably due to Ti–O–N–C, Ti–O–C and hydrogen bonding between surface hydroxyl groups of TiO$_2$ and protonated nitrogen atoms of PANI.

UV-DRS Analysis

UV-DRS spectra of TiO$_2$ and PANI-TiO$_2$ composites were shown in Fig. 13a-c. The maximum reflectance of TiO$_2$ observed at about 410 nm could absorb only UV light. On the other hand, PANI-TiO$_2$ composites exhibited a reflectance both in UV and visible region. Notably, this red shift originated from the band gap narrowing of TiO$_2$ by surface modification due to the presence of PANI. The reflectance pattern of PANI-TiO$_2$ composites, especially with higher PANI ratios, indicated divergence to visible light

region. PANI-TiO$_2$ composites evidently exhibited bands corresponding to PANI as the bands at around 360 nm and 480 nm were the characteristic bands related to the benzenoid π-π* transition and polaron→π* transition, respectively (Karaoğlan and Bindal 2018; Radoičić et al. 2012, 2013). The red shift of these bands in PANI-TiO$_2$ composites could be interpreted as the result of an interruption of π-π* or polaron→π* transition through the association of PANI with TiO$_2$. UV-DRS spectra of PT-81 expressed an endless long tail starting from 660 nm following the third characteristic band of PANI at 632 nm. This tail band was assigned to the extended delocalization of electrons arising from the strong interactions between the PANI chain and TiO$_2$, resulting in the formation of a polaron structure. As PANI concentration decreased in PANI-TiO$_2$ composites, the intensity and tailing trend reduced due to the declining tendency of isolated polarons (Dinooplal et al. 2021). This result was consistent with FTIR-ATR and Raman data showing that the polarons decreased in PANI-TiO$_2$ composites. Although a typical *in-situ* chemical oxidation polymerization method was applied, the band gap energy of PANI displayed variations in the range of 1.38–2.40 eV, the reason of which
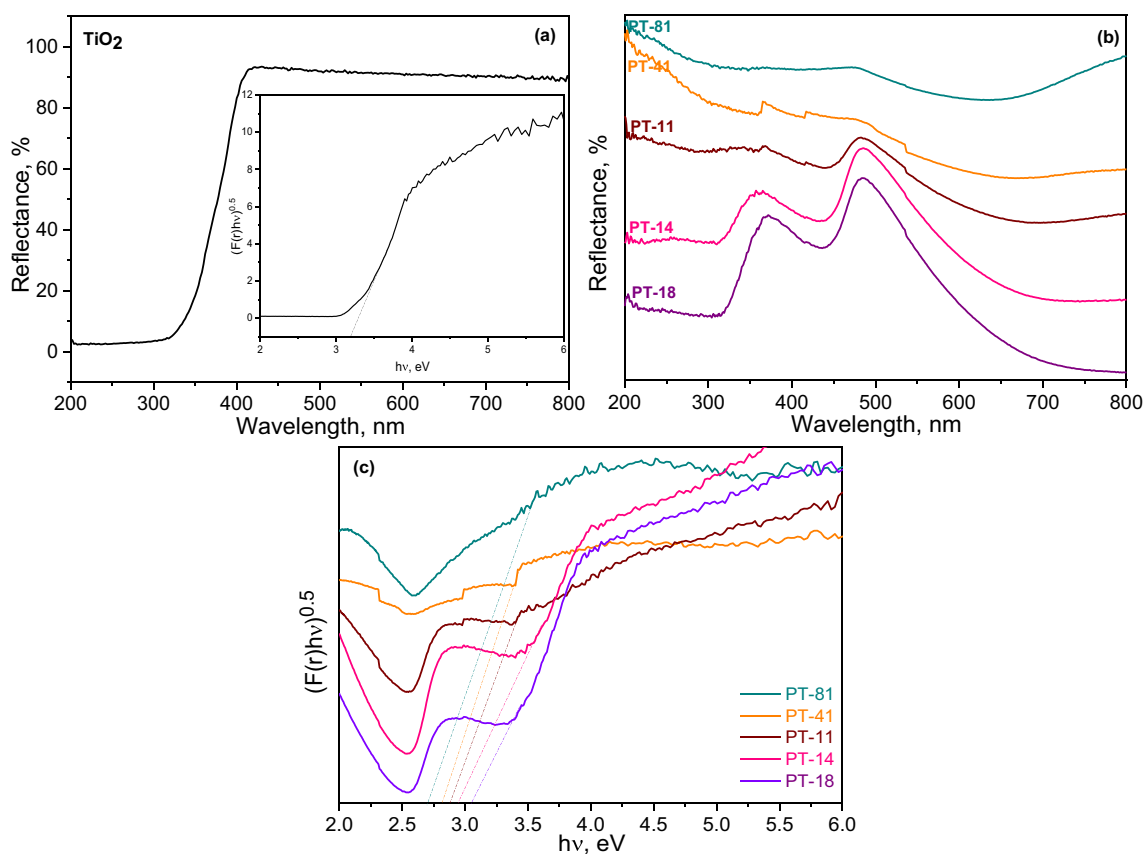
Fig. 13 (**a**) UV-DRS spectra of TiO$_2$ and (F(R).hν)$^{0.5}$ v/s hν plot (inserted), (**b**) UV-DRS spectra of PANI-TiO$_2$ composites (**c**) (F(R).hν)$^{0.5}$ v/s hν plot of PANI-TiO$_2$ composites

could be attributed to the minor modifications such as the selection of dopant agents, *i.e.*, HCl or H$_2$SO$_4$ (Karaoğlan and Bindal 2018; Rahman and Kar 2020a, b; Yang et al. 2017). The calculated band gap energies of PT-81, PT-41, PT-11, PT-14, PT-18, TiO$_2$ were 2.71 eV, 2.82 eV, 2.90 eV, 2.96 eV, 3.06 eV, 3.20 eV, respectively. Coupling of TiO$_2$ with PANI caused a reduction in band gap energies of PANI-TiO$_2$ composites thereby enabling visible light absorption and leading to the successful utilization of solar irradiation.

PL Analysis

PL spectra of TiO$_2$ and selected PANI-TiO$_2$ composites (PT-11, PT-14 and PT-41) were presented in Fig. 14. Three emission peaks of TiO$_2$ were located at 384 nm, 459 nm, and 553 nm. The first strong emission peak at 384 nm corresponded to pure TiO$_2$ anatase phase and was assigned to the band edge emission revealing the band gap of TiO$_2$. The peaks at 459 nm and 553 nm were related to surface state emissions originating from the recombination of trapped electron–hole pairs due to the dangling bonds of TiO$_2$ (Jho et al. 2008; Mathew et al. 2012). A red shift was noted in the most intense peak with increasing
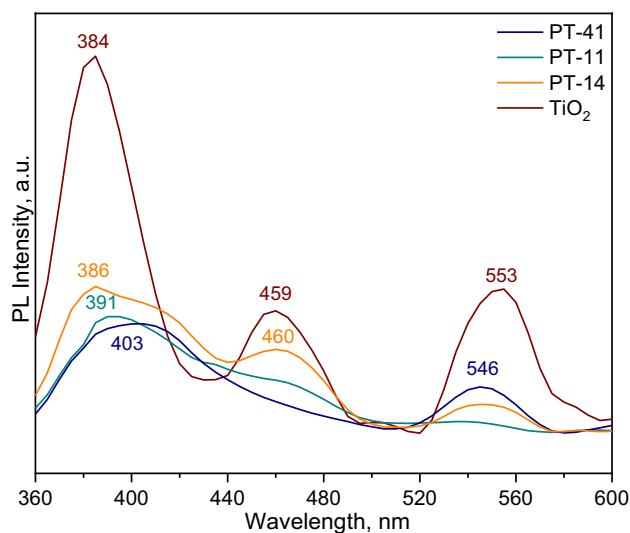

Fig. 14 PL spectra of TiO$_2$ and PANI-TiO$_2$ composites

PANI ratio in the composites. This emission peak was observed at 386 nm, 391 nm, and 403 nm for PT-14, PT-11, PT41 specimens, respectively. The PL emission
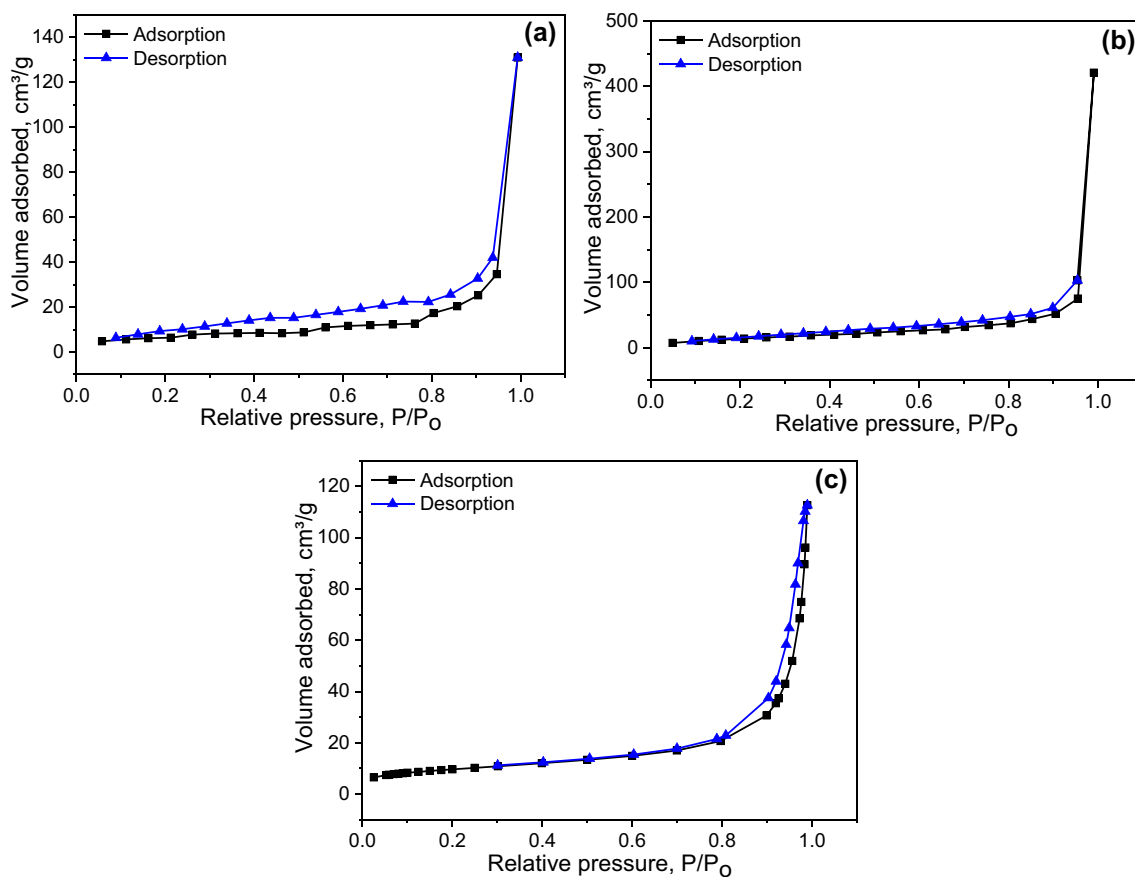
Fig. 15 Nitrogen isotherms of (**a**) PANI, (**b**) TiO_2, (**c**) PT-11

intensities of PANI-TiO_2 composites also decreased considerably in comparison to PL emission intensity of TiO_2. The reason could be the reduction of the recombination rate of trapped electron–hole pair resulting in charge separation possibly leading to enhancement in photocatalytic activity (Merangmenla et al. 2022; Sambaza et al. 2020). Higher PL signals recorded due to the presence of various defects and/or oxygen vacancies could also affect the photocatalytic activity (Yurdakal et al. 2019). Both PL and UV-DRS analyses confirmed the band-gap reduction phenomenon of PANI modification of TiO_2.

Nitrogen physisorption analysis

Nitrogen isotherms of bare PANI, TiO_2 and PT-11 specimens were displayed in Fig. 15a-c. The effect of PANI modification on surface area properties of TiO_2 composites could well be characterized by PT-11 composite. Generally, Type III isotherms expressed low adsorption capacity whereas most catalysts revealed Type IV isotherms (Yurdakal et al. 2019). The isotherm of PANI specimen revealed Type III, while PT-11 specimen

displayed Type IV isotherm with H4 type hysteresis loop according to IUPAC-BET classification (Sing 1985). Besides, TiO_2 catalyst resembled a hysteresis curve of Type IV at relative pressures greater than $p/p_0 = 0.50$ (Fig. 15b). S_{BET} of bare PANI, TiO_2, and PT-11 were 26 m^2/g, 57 m^2/g, and 34 m^2/g, respectively. Different S_{BET} of PANI as 19–21 m^2/g even a drastically smaller surface area as ~ 4 m^2/g were reported by various research groups (Deng et al. 2016; Sambaza et al. 2020; Wang et al. 2019). The incorporation of PANI into TiO_2 resulted in a reduction of surface area of TiO_2 most probably due to surface coverage. This change in morphology was observed by SEM micrograph of PT-11 composite (Fig. 6d). The BJH pore diameters of PANI, TiO_2, and PT-11 were found as 22.5 nm, 14.4 nm, and 20.3 nm, respectively expressing mesoporous structure. Sample specific pore size variations were also reported in the range of 20–35 nm the reason for which could be attributed to the diverse morphological character of the composites depending on the preparation methodology (Guo et al. 2014; Kong et al. 2019; Sambaza et al. 2020; Wang et al. 2019).
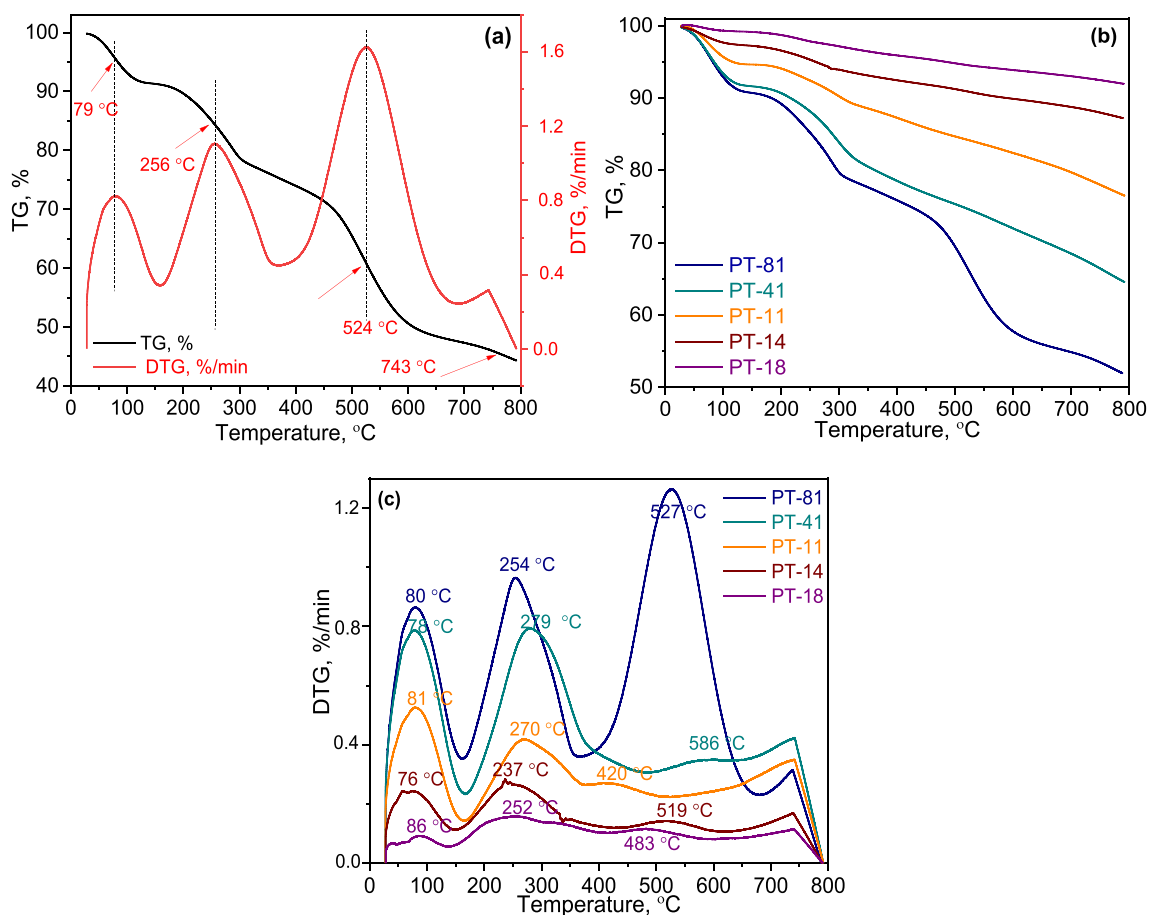
Fig. 16 TG and DTG curves of (**a**) PANI, (**b**) TG and (**c**) DTG curves of synthesized PANI-TiO$_2$ composites

Thermogravimetric analysis

Thermogravimetric data were presented as TG curve or alternatively as a derivative thermogravimetric (DTG) curve, which is a plot of the rate of change of mass against temperature. TG and DTG profiles of bare PANI and PANI-TiO$_2$ composites were acquired to investigate the stability of PANI and the thermal decomposition of the composites. All specimens showed four major weight loss steps (Fig. 16a-c).

The relatively small weight loss at temperatures lower than 120 °C was typically attributed to the volatile components and especially to the adsorbed water. Therefore, the initial 4.4% weight loss at around 80 °C was related to the removal of adsorbed water molecules on bare PANI (Fig. 16a). The additional weight loss of PANI at a temperature in the range of 165–360 °C was attributed to the elimination of impurities, small-chain oligomers and/or dopants. This additional weight loss, peaking at around 256 °C was 11.2%. The total weight loss up to this point accounted as 15.6%. The major weight loss beyond this temperature, peaking at 524 °C was assigned to the decomposition of the polymer. A significant mass loss occurred in temperatures

between 405 °C and 675 °C, expressing an additional 23.3% decrease of weight (Gomes and Oliveira 2012; Lin et al. 2012; Yue et al. 1991). An initial stage of PANI carbonization could be detected under an inert (nitrogen) atmosphere beyond 700 °C (Gomes and Oliveira 2012).

TG and DTG curves of PANI-TiO$_2$ composites were illustrated in Fig. 16b and c, respectively. The degradation curves of PT-81 and PT-41 composites were similar to that of PANI. The initial mass loss of PANI-TiO$_2$ composites was attributed to the removal of moisture, and thereafter the peaks appeared between 240 °C and 280 °C with changing PANI amounts in composites due to the elimination of dopant and/or low molecular weight oligomers as expected. The curves showed that the main mass loss occurred around 400 °C and continued until 670 °C indicating the decomposition of the skeletal polyaniline chain structure (Sui et al. 2004; Yang et al. 2017). A noticeable drop was observed in the decomposition temperature of the PT-11 composite (420 °C) compared to bare PANI (524 °C). The decrement in thermal decomposition temperature could indicate a weakened interactive force within PANI chains due to a strong interaction that occurred at

the interface of TiO$_2$ and PANI. This situation could lead to the thermal decomposition of PANI in composites at low temperatures (Li et al. 2003; Pham et al. 2009). The weight loss of composites with an increasing amount of TiO$_2$ decreased gradually, as expected, due to the dilution effect of the inert oxide particles. Total weight losses were determined as 55.7%, 48.1%, 35.5%, 23.5%, 12.8%, and 8.00% for bare PANI, PT-81, PT-41, PT-11, PT-14, and PT-18, respectively. In general, PANI-TiO$_2$ composites were found to exhibit similar thermal stabilities as bare PANI. The concentration and chemical structure of PANI on TiO$_2$ particles could possibly affect the degradation rate of PANI. Moreover, PANI degradation rate was 1.63%/min that gradually decreased with increasing TiO$_2$ content in the composites. The degradation rates of PANI in composites were 1.3%/min, 0.35%/min, 0.27%/min, 0.14%/min, and 0.12%/min for PT-81, PT-41, PT-11, PT-14, and PT-18 composites, respectively. This situation showed that no imperfection such as distortion in chain symmetry affecting adversely the delocalized system was observed due to the increase in PANI ratio of composites (Bhadra et al. 2007; Gilja et al. 2017).

Conclusions

This study focused on the preparation of PANI and PANI-TiO$_2$ composites by *in-situ* chemical oxidation polymerization method. The structure of PANI-TiO$_2$ composites was systematically investigated by various characterization techniques confirming the successful formation of the composite. XRD patterns indicated the presence of anatase and rutile phases of TiO$_2$ and the amorphous nature of PANI in composites. Moreover, the surface modification of TiO$_2$ by PANI exerted no remarkable effect on the lattice structure of TiO$_2$ particles. SEM analysis specified that PANI was consistently deposited on the surface of slightly agglomerated/aggregated TiO$_2$ particles. The decreasing trend of the band gap (from 3.06 eV to 2.71 eV) with increasing PANI ratios in the composites indicated a shift of the absorption spectra from UV to the visible region. TG and DTG analyses showed that PANI-TiO$_2$ composites in general exhibited similar thermal stabilities as PANI. Furthermore, the photocatalyst specimens were further characterized under pre- and post-photocatalytic conditions in a comparative manner. Under post-photocatalytic conditions, the structural and morphological stability of PANI and PANI-TiO$_2$ composites in the presence of RfOM was confirmed by FTIR-ATR, Raman spectroscopy, XRD, and SEM-EDAX techniques. This study was conducted to provide a new insight in the field of photocatalysis. In that respect, a conducting polymer such as PANI and an inorganic semiconductor such as TiO$_2$ were combined to prepare a novel photocatalyst and

tested for the removal of a model RfOM, namely HA under solar light. Based on these findings both presented here and elsewhere (Uyguner-Demirel et al. 2023), PANI-TiO$_2$ composites were proven to be suitable for alternative solar photocatalytic applications overcoming the limitations of UVA light active bare TiO$_2$ photocatalysis. The utilization of PANI-TiO$_2$ composites as an inexpensive and environmentally friendly photocatalyst in drinking water supply treatment processes can be a significant and potential option for the efficient removal of RfOM.

Declarations

References

Anirudhan TS, Manjusha V, Shainy F (2021) Magnetically retrievable cysteine modified graphene oxide@nickelferrite@titanium dioxide photocatalyst for the effective degradation of chlorpyrifos from aqueous solutions. Environ Technol Innov 23:101633. https://doi.org/10.1016/j.eti.2021.101633

Bessergenev VG, Mateus MC, do Rego AMB, Hantusch M, Burkel E (2015) An improvement of photocatalytic activity of TiO$_2$ Degussa P25 powder. Appl Catal A 500:40–50. https://doi.org/10.1016/j.apcata.2015.05.002

Bhadra S, Singha NK, Khastgir D (2007) Electrochemical synthesis of polyaniline and its comparison with chemically synthesized polyaniline. J Appl Polym Sci 104:1900–1904. https://doi.org/10.1002/app.25867

Bhandari S (2018) Chapter 2 - Polyaniline: Structure and properties relationship. In: Visakh PM, Pina CD, Falletta E (eds) Polyaniline blends, composites, and nanocomposites, 1st edn. Elsevier, Amsterdam, pp 23–60

Bláha M, Trchová M, Bober P, Morávková Z, Prokeš J, Stejskal J (2017) Polyaniline: Aniline oxidation with strong and weak oxidants under various acidity. Mater Chem Phys 194:206–218. https://doi.org/10.1016/j.matchemphys.2017.03.028

Cionti C, Della Pina C, Meroni D, Falletta E, Ardizzone S (2020) Photocatalytic and Oxidative Synthetic Pathways for Highly Efficient PANI-TiO$_2$ nanocomposites as organic and inorganic pollutant sorbents. Nanomaterials 10:441. https://doi.org/10.3390/nano10030441

Cullity BD, Stock SR (2014) Elements of X-Ray Diffraction. Pearson Education Limited, Edinburgh

Das HT, Dutta S, Beura R, Das N (2022) Role of polyaniline in accomplishing a sustainable environment: recent trends in polyaniline for eradicating hazardous pollutants. Environ Sci Pollut Res 29:49598–49631. https://doi.org/10.1007/s11356-022-20916-5

Deng Y, Tang L, Zeng G, Dong H, Yan M, Wang J, Hu W, Wang J, Zhou Y, Tang J (2016) Enhanced visible light photocatalytic performance of polyaniline modified mesoporous single crystal TiO$_2$ microsphere. Appl Surf Sci 387:882–893. https://doi.org/10.1016/j.apsusc.2016.07.026

Dinoopal S, Sunil Jose T, Rajesh C, Anju Rose Puthukkara P, SavithaUnnikrishnan K, Arun KJ (2021) Accelerated photodegradation of polystyrene by TiO$_2$-polyaniline photocatalyst under UV radiation. Eur Polym J 153:110493. https://doi.org/10.1016/j.eurpolymj.2021.110493

Djaballah AM, Bellardita M, Palmisano L, Loddo V, Umair M, Pecoraro CM, Bagtache R, Trari M (2023) Facile preparation of CuBi$_2$O$_4$/TiO$_2$ hetero-systems employed for simulated solar-light selective oxidation of 4-methoxybenzyl alcohol model compound. Mol Catal 546:113251. https://doi.org/10.1016/j.mcat.2023.113251

Doğan D, Taş R, Can M (2020) Increasing Photocatalytic Stability and Photocatalytic Property of Polyaniline Conductive Polymer. Iran J Sci Technol Trans a: Sci 44:1025–1037. https://doi.org/10.1007/s40995-020-00922-3

Eftekhari A (2010) Nanostructured Conductive Polymers. John Wiley & Sons Ltd, West Sussex, United Kingdom

Emeline AV, Kuznetsov VN, Ryabchuk VK, Serpone N (2012) On the way to the creation of next generation photoactive materials. Environ Sci Pol Res 19:3666–3675. https://doi.org/10.1007/s11356-011-0665-3

Enesca A, Cazan C (2022) Polymer Composite-based materials with photocatalytic applications in wastewater organic pollutant removal: A mini review. Polymers 14:3291. https://doi.org/10.3390/polym14163291

Francioso O, Sanchez-Cortes S, Tugnoli V, Ciavatta C, Sitti L, Gessa C (1996) Infrared, Raman, and Nuclear Magnetic Resonance (^{1}H, ^{13}C, and ^{31}P) spectroscopy in the study of fractions of peat humic acids. Appl Spectrosc 50:1165–1174

Frimmel FH, Abbt-Braun G, Heumann KG, Hock B, Lüdemann H-D, Spiteller M (2008) Refractory organic substances in the environment. Weinheim, Germany

Fujishima A, Honda K (1972) Electrochemical photolysis of water at a semiconductor electrode. Nature 238:37–38. https://doi.org/10.1038/238037a0

Gilja V, Novaković K, Travas-Sejdic J, Hrnjak-Murgić Z, Kraljić Roković M, Žic M (2017) Stability and synergistic effect of polyaniline/TiO$_2$ photocatalysts in degradation of azo dye in wastewater. Nanomaterials 7:412. https://doi.org/10.3390/nano7120412

Golczak S, Kanciurzewska A, Fahlman M, Langer K, Langer JJ (2008) Comparative XPS surface study of polyaniline thin films. Solid State Ion 179:2234–2239. https://doi.org/10.1016/j.ssi.2008.08.004

Gomes EC, Oliveira MAS (2012) Chemical polymerization of aniline in hydrochloric acid (HCl) and formic acid (HCOOH) media. Differences between the two synthesized polyanilines. J Appl Polym Sci 2:5–13. https://doi.org/10.5923/j.ajps.20120202.02

Gospodinova N, Terlemezyan L (1998) Conducting polymers prepared by oxidative polymerization: polyaniline. Prog Polym Sci 23:1443–1484. https://doi.org/10.1016/S0079-6700(98)00008-2

Gu L, Wang J, Qi R, Wang X, Xu P, Han X (2012a) A novel incorporating style of polyaniline/TiO$_2$ composites as effective visible photocatalysts. J Mol Catal a: Chem 357:19–25. https://doi.org/10.1016/j.molcata.2012.01.012

Gu H, Rapole SB, Sharma J, Huang Y, Cao D, Colorado HA, Luo Z, Haldolaarachchige N, Young DP, Walters B, Wei S, Guo Z (2012b) Magnetic polyaniline nanocomposites toward toxic hexavalent chromium removal. RSC Adv 2:11007–11018. https://doi.org/10.1039/C2RA21991C

Guo N, Liang Y, Lan S, Liu L, Zhang J, Ji G, Gan S (2014) Microscale hierarchical three-dimensional flowerlike TiO$_2$/PANI composite: Synthesis, characterization, and its remarkable photocatalytic activity on organic dyes under UV-light and sunlight irradiation. J Phys Chem C 118:18343–18355. https://doi.org/10.1021/jp5044927

Hatchard CG, Parker CA (1956) A new sensitive chemical actinometer-II. Potassium ferrioxalate as a standard chemical actinometer. Proc R Soc Lond A 235:518–536. https://doi.org/10.1098/rspa.1956.0102

Jeong W-H, Amna T, Ha Y-M, Hassan MS, Kim H-C, Khil M-S (2014) Novel PANI nanotube@TiO$_2$ composite as efficient chemical and biological disinfectant. Chem Eng J 246:204–210. https://doi.org/10.1016/j.cej.2014.02.054

Jho JH, Kim DH, Kim S-J, Lee KS (2008) Synthesis and photocatalytic property of a mixture of anatase and rutile TiO$_2$ doped with Fe by mechanical alloying process. J Alloys Compd 459:386–389. https://doi.org/10.1016/j.jallcom.2007.04.285

Jumat NA, Wai PS, Ching JJ, Basirun WJ (2017) Synthesis of polyaniline-TiO$_2$ nanocomposites and their application in photocatalytic degradation. Polym Polym Compos 25:507–514. https://doi.org/10.1177/096739111702500701

Kang ET, Neoh KG, Tan KL (1998) Polyaniline: A polymer with many interesting intrinsic redox states. Prog Polym Sci 23:277–324. https://doi.org/10.1016/S0079-6700(97)00030-0

Karaoğlan N, Bindal C (2018) Synthesis and optical characterization of benzene sulfonic acid doped polyaniline. Eng Sci Technol Int J 21:1152–1158. https://doi.org/10.1016/j.jestch.2018.09.010

Kong P, Liu P, Ge Z, Tan H, Pei L, Wang J, Zhu P, Gu X, Zheng Z, Li Z (2019) Conjugated HCl-doped polyaniline for photocatalytic oxidative coupling of amines under visible light. Catal Sci Technol 9:753–761. https://doi.org/10.1039/C8CY02280A

Koysuren O, Koysuren HN (2019) Photocatalytic activity of polyaniline/Fe-doped TiO$_2$ composites by in situ polymerization method. J Macromol Sci A 56:1–10. https://doi.org/10.1080/10601325.2019.1565548

Kulkarni SB, Navale YH, Navale ST, Stadler FJ, Ramgir NS, Patil VB (2019) Hybrid polyaniline-WO$_3$ flexible sensor: A room temperature competence towards NH$_3$ gas. Sens Actuators B Chem 288:279–288. https://doi.org/10.1016/j.snb.2019.02.094

Kumar SN, Bouyssoux G, Gaillard F (1990) Electronic and structural characterization of electrochemically synthesized conducting polyaniline from XPS studies. Surf Interface Anal 15:531–536. https://doi.org/10.1002/sia.740150906

Lee Y-J, Lee HS, Lee C-G, Park S-J, Lee J, Jung S, Shin G-A (2020) Application of PANI/TiO$_2$ composite for photocatalytic degradation of contaminants from aqueous solution. Appl Sci 10:6710. https://doi.org/10.3390/app10196710

Li X, Chen W, Bian C, He J, Xu N, Xue G (2003) Surface modification of TiO$_2$ nanoparticles by polyaniline. Appl Surf Sci 217:16–22. https://doi.org/10.1016/S0169-4332(03)00565-8

Li X, Wang D, Cheng G, Luo Q, An J, Wang Y (2008a) Preparation of polyaniline-modified TiO$_2$ nanoparticles and their photocatalytic activity under visible light illumination. Appl Catal B 81:267–273. https://doi.org/10.1016/j.apcatb.2007.12.022

Li X, Wang D, Luo Q, An J, Wang Y, Cheng G (2008b) Surface modification of titanium dioxide nanoparticles by polyaniline via an *in*

situ method. J Chem Technol Biotechnol 83:1558–1564. https://doi.org/10.1002/jctb.1970

Li Q, Sun L, Zhang Y, Qian Y, Zhai J (2011) Characteristics of equilibrium, kinetics studies for adsorption of Hg(II) and Cr(VI) by polyaniline/humic acid composite. Desalination 266:188–194. https://doi.org/10.1016/j.desal.2010.08.025

Li Y, Yu Y, Wu L, Zhi J (2013) Processable polyaniline/titania nanocomposites with good photocatalytic and conductivity properties prepared via peroxo-titanium complex catalyzed emulsion polymerization approach. Appl Surf Sci 273:135–143. https://doi.org/10.1016/j.apsusc.2013.01.213

Li R, Li T, Zhou Q (2020) Impact of titanium dioxide (TiO$_2$) modification on its application to pollution treatment—A review. Catalysts 10:804. https://doi.org/10.3390/catal10070804

Liao G, Chen S, Quan X, Zhang Y, Zhao H (2011) Remarkable improvement of visible light photocatalysis with PANI modified core–shell mesoporous TiO$_2$ microspheres. Appl Catal B 102:126–131. https://doi.org/10.1016/j.apcatb.2010.11.033

Lin Y, Li D, Hu J, Xiao G, Wang J, Li W, Fu X (2012) Highly Efficient Photocatalytic Degradation of Organic Pollutants by PANI-Modified TiO$_2$ Composite. J Phys Chem C 116:5764–5772. https://doi.org/10.1021/jp211222w

Mathew S, Kumar Prasad A, Benoy T, Rakesh PP, Hari M, Libish TM, Radhakrishnan P, Nampoori VPN, Vallabhan CPG (2012) UV-visible photoluminescence of TiO$_2$ nanoparticles prepared by hydrothermal method. J Fluoresc 22:1563–1569. https://doi.org/10.1007/s10895-012-1096-3

Merangmenla NB, Baruah S, Puzari A (2022) 1D copper (II) based coordination polymer/PANI composite fabrication for enhanced photocatalytic activity. J Photochem Photobiol A 427:113803. https://doi.org/10.1016/j.jphotochem.2022.113803

Monfared AH, Jamshidi M (2019) Synthesis of polyaniline/titanium dioxide nanocomposite (PAni/TiO$_2$) and its application as photocatalyst in acrylic pseudo paint for benzene removal under UV/VIS lights. Prog Org Coat 136:105257. https://doi.org/10.1016/j.porgcoat.2019.105257

Nakata K, Fujishima A (2012) TiO$_2$ photocatalysis: Design and applications. J Photochem Photobiol c: Photochem Rev 13:169–189. https://doi.org/10.1016/j.jphotochemrev.2012.06.001

Ohsaka T, Izumi F, Fujiki Y (1978) Raman spectrum of anatase, TiO$_2$. J Raman Spectrosc 7:321–324. https://doi.org/10.1002/jrs.1250070606

Oyetade JA, Machunda RL, Hilonga A (2022) Photocatalytic degradation of azo dyes in textile wastewater by Polyaniline composite catalyst-a review. Sci Afr 17:e01305. https://doi.org/10.1016/j.sciaf.2022.e01305

Pal R, Goyal SL, Rawal I (2020) High-performance solid state supercapacitors based on intrinsically conducting polyaniline/MWCNTs composite electrodes. J Polym Res 27:179. https://doi.org/10.1007/s10965-020-02144-y

Pawar SG, Patil SL, Chougule MA, Achary SN, Patil VB (2010) Microstructural and optoelectronic studies on polyaniline: TiO$_2$ nanocomposites. Int J Polym Mater Polym Biomater 60:244–254. https://doi.org/10.1080/00914037.2010.504175

Pawar SG, Patil SL, Chougule MA, Raut BT, Sen S, Patil VB (2011) camphor sulfonic acid doped polyaniline-titanium dioxide nanocomposite: Synthesis, structural, morphological, and electrical properties. Int J Polym Mater Polym Biomater 60:979–987. https://doi.org/10.1080/00914037.2011.553848

Pawar TJ, Contreras López D, Olivares Romero JL, Vallejo Montesinos J (2023) Surface modification of titanium dioxide. J Mater Sci 58:6887–6930. https://doi.org/10.1007/s10853-023-08439-x

Pham QM, Pham DH, Kim J-S, Kim EJ, Kim S (2009) Preparation of polyaniline–titanium dioxide hybrid materials in supercritical CO$_2$. Synth Met 159:2141–2146. https://doi.org/10.1016/j.synthmet.2009.08.003

Porcu S, Secci F, Ricci PC (2022) Advances in hybrid composites for photocatalytic applications: A review. Molecules 27:6828. https://doi.org/10.3390/molecules27206828

Preethika M, Sundramoorthy AK (2019) Humic acid/halloysite nanotube/flavin adenine dinucleotide nanocomposite based selective electrochemical biosensor for hydrogen peroxide. Appl Surf Sci 488:503–511. https://doi.org/10.1016/j.apsusc.2019.05.255

Radoičić M, Šaponjić Z, Ćirić-Marjanović G, Konstantinović Z, Mitrić M, Nedeljković J (2012) Ferromagnetic polyaniline/TiO$_2$ nanocomposites. Polym Compos 33:1482–1493. https://doi.org/10.1002/pc.22278

Radoičić M, Šaponjić Z, Janković IA, Ćirić-Marjanović G, Ahrenkiel SP, Čomor MI (2013) Improvements to the photocatalytic efficiency of polyaniline modified TiO$_2$ nanoparticles. Appl Catal B 136–137:133–139. https://doi.org/10.1016/j.apcatb.2013.01.007

Rahman KH, Kar AK (2020a) Titanium-di-oxide (TiO$_2$) concentration-dependent optical and morphological properties of PAni-TiO$_2$ nanocomposite. Mater Sci Semicond Process 105:104745. https://doi.org/10.1016/j.mssp.2019.104745

Rahman KH, Kar AK (2020b) Effect of band gap variation and sensitization process of polyaniline (PANI)-TiO$_2$ p-n heterojunction photocatalysts on the enhancement of photocatalytic degradation of toxic methylene blue with UV irradiation. J Environ Chem Eng 8:104181. https://doi.org/10.1016/j.jece.2020.104181

Reddy KR, Hassan M, Gomes VG (2015) Hybrid nanostructures based on titanium dioxide for enhanced photocatalysis. Appl Catal A 489:1–16. https://doi.org/10.1016/j.apcata.2014.10.001

Reddy KR, Karthik KV, Prasad SBB, Soni SK, Jeong HM, Raghu AV (2016) Enhanced photocatalytic activity of nanostructured titanium dioxide/polyaniline hybrid photocatalysts. Polyhedron 120:169–174. https://doi.org/10.1016/j.poly.2016.08.029

Rehman ZU, Bilal M, Hou J, Butt FK, Ahmad J, Ali S, Hussain A (2022) Photocatalytic CO$_2$ reduction using TiO$_2$-based photocatalysts and TiO$_2$ Z-scheme heterojunction composites: A review. Molecules 27:2069. https://doi.org/10.3390/molecules27072069

Rodríguez FJ, Schlenger P, García-Valverde M (2016) Monitoring changes in the structure and properties of humic substances following ozonation using UV–vis, FTIR and 1H NMR techniques. Sci Total Environ 541:623–637. https://doi.org/10.1016/j.scitotenv.2015.09.127

Sambaza SS, Maity A, Pillay K (2020) Polyaniline-coated TiO$_2$ nanorods for photocatalytic degradation of bisphenol A in Water. ACS Omega 5:29642–29656. https://doi.org/10.1021/acsomega.0c00628

Sánchez-Cortés S, Francioso O, Ciavatta C, García-Ramos JV, Gessa C (1998) pH-dependent adsorption of fractionated peat humic substances on different silver colloids studied by surface-enhanced Raman spectroscopy. J Colloid Interface Sci 198:308–318. https://doi.org/10.1006/jcis.1997.5293

Sánchez-Cortés S, Corrado G, Trubetskaya OE, Trubetskoj OA, Hermosin B, Saiz-Jimenez C (2006) Surface-enhanced raman spectroscopy of chernozem humic acid and their fractions obtained by coupled size exclusion chromatography-polyacrylamide gel electrophoresis (SEC-PAGE). Appl Spectrosc 60:48–53. https://doi.org/10.1366/000370206775382695

Sandikly N, Kassir M, El Jamal M, Takache H, Arnoux P, Mokh S, Al-Iskandarani M, Roques-Carmes T (2021) Comparison of the toxicity of waters containing initially sulfaquinoxaline after photocatalytic treatment by TiO$_2$ and polyaniline/TiO$_2$. Environ Technol 42:419–428. https://doi.org/10.1080/09593330.2019.1630485

Sarmah S, Kumar A (2011) Photocatalytic activity of polyaniline-TiO$_2$ nanocomposites. Indian J Phys 85:713–726. https://doi.org/10.1007/s12648-011-0071-1

Sboui M, Nsib MF, Rayes A, Swaminathan M, Houas A (2017) TiO$_2$–PANI/Cork composite: A new floating photocatalyst for the treatment of organic pollutants under sunlight irradiation. J Environ Sci 60:3–13. https://doi.org/10.1016/j.jes.2016.11.024

Scherrer P (1918) Estimation of the size and internal structure of colloidal particles by means of röntgen. Nachr Ges Wiss Gottingen 2:96–100

Senesi N, D'Orazio V, Ricca G (2003) Humic acids in the first generation of EUROSOILS. Geoderma 116:325–344. https://doi.org/10.1016/S0016-7061(03)00107-1

Sing KSW (1985) Reporting physisorption data for gas/solid systems with special reference to the determination of surface area and porosity (Recommendations 1984). Pure Appl Chem 57:603–619. https://doi.org/10.1351/pac198557040603

Singh P, Shukla SK (2020) Advances in polyaniline-based nanocomposites. J Mater Sci 55:1331–1365. https://doi.org/10.1007/s10853-019-04141-z

Singh S, Mahalingam H, Singh PK (2013) Polymer-supported titanium dioxide photocatalysts for environmental remediation: A review. Appl Catal A 462–463:178–195. https://doi.org/10.1016/j.apcata.2013.04.039

Singh S, Perween S, Ranjan A (2021) Dramatic enhancement in adsorption of congo red dye in polymer-nanoparticle composite of polyaniline-zinc titanate. J Environ Chem Eng 9:105149. https://doi.org/10.1016/j.jece.2021.105149

Spurr RA, Myers H (1957) Quantitative analysis of anatase-rutile mixtures with an X-Ray Diffractometer. Anal Chem 29:760–762. https://doi.org/10.1021/ac60125a006

Stejskal J (2020) Interaction of conducting polymers, polyaniline and polypyrrole, with organic dyes: polymer morphology control, dye adsorption and photocatalytic decomposition. Chem Pap 74:1–54. https://doi.org/10.1007/s11696-019-00982-9

Stejskal J, Riede A, Hlavatá D, Prokeš J, Helmstedt M, Holler P (1998) The effect of polymerization temperature on molecular weight, crystallinity, and electrical conductivity of polyaniline. Synth Met 96:55–61. https://doi.org/10.1016/S0379-6779(98)00064-2

Subramanian E, Subbulakshmi S, Murugan C (2014) Inter-relationship between nanostructures of conducting polyaniline and the photocatalytic methylene blue dye degradation efficiencies of its hybrid composites with anatase TiO_2. Mater Res Bull 51:128–135. https://doi.org/10.1016/j.materresbull.2013.12.006

Sui X, Chu Y, Xing S, Yu M, Liu C (2004) Self-organization of spherical $PANI/TiO_2$ nanocomposites in reverse micelles. Colloids Surf a: Physicochem Eng Asp 251:103–107. https://doi.org/10.1016/j.colsurfa.2004.08.015

Tan KL, Tan BTG, Kang ET, Neoh KG (1989) X-ray photoelectron spectroscopy studies of the chemical structure of polyaniline. Phys Rev B 39:8070–8073. https://doi.org/10.1103/PhysRevB.39.8070

Tang Q, Wu J, Sun H, Lin J, Fan S, Hu D (2008) Polyaniline/polyacrylamide conducting composite hydrogel with a porous structure. Carbohydr Polym 74:215–219. https://doi.org/10.1016/j.carbpol.2008.02.008

Tao S, Hong B, Kerong Z (2007) An infrared and Raman spectroscopic study of polyanilines co-doped with metal ions and H^+. Spectrochim Acta A Mol Biomol Spectrosc 66:1364–1368. https://doi.org/10.1016/j.saa.2006.08.011

Turkten N, Karatas Y, Bekbolet M (2021) Conducting polymers and photocatalysis: A mini review on selected conducting polymers and photocatalysts as TiO_2 and ZnO. J Photocatal 2:252–270. https://doi.org/10.2174/2665976X02666211201121530

Uyguner-Demirel CS, Turkten N, Kaya D, Bekbolet M (2022) Effect of oxidative and non-oxidative conditions on molecular size fractionation of humic acids: TiO_2 and Cu-doped TiO_2 photocatalysis. Environ Sci Pollut Res 29:85413–85432. https://doi.org/10.1007/s11356-022-21754-1

Uyguner-Demirel CS, Turkten N, Karatas Y, Bekbolet M (2023) Photocatalytic performance of PANI modified TiO_2: Degradation of refractory organic matter. Environ Sci Pollut Res 30:85626–85638. https://doi.org/10.1007/s11356-023-28385-0

Wan M (2008) Conducting Polymers with micro or nanometer structure. Springer, New York

Wang F, Min S, Han Y, Feng L (2010) Visible-light-induced photocatalytic degradation of methylene blue with polyaniline-sensitized TiO_2 composite photocatalysts. Superlattices Microstruct 48:170–180. https://doi.org/10.1016/j.spmi.2010.06.009

Wang Z, Peng X, Huang C, Chen X, Dai W, Fu X (2017) CO gas sensitivity and its oxidation over TiO_2 modified by PANI under UV irradiation at room temperature. Appl Catal B 219:379–390. https://doi.org/10.1016/j.apcatb.2017.07.080

Wang N, Chen J, Wang J, Feng J, Yan W (2019) Removal of methylene blue by Polyaniline/TiO_2 hydrate: Adsorption kinetic, isotherm and mechanism studies. Powder Technol 347:93–102. https://doi.org/10.1016/j.powtec.2019.02.049

Wang H, Li X, Zhao X, Li C, Song X, Zhang P, Huo P, Li X (2022) A review on heterogeneous photocatalysis for environmental remediation: From semiconductors to modification strategies. Chinese J Catal 43:178–214. https://doi.org/10.1016/S1872-2067(21)63910-4

Yalçın Y, Kılıç M, Çınar Z (2010) Fe^{+3}-doped TiO_2: A combined experimental and computational approach to the evaluation of visible light activity. Appl Catal B 99:469–477. https://doi.org/10.1016/j.apcatb.2010.05.013

Yang C, Dong W, Cui G, Zhao Y, Shi X, Xia X, Tang B, Wang W (2017) Enhanced photocatalytic activity of PANI/TiO_2 due to their photosensitization-synergetic effect. Electrochim Acta 247:486–495. https://doi.org/10.1016/j.electacta.2017.07.037

Yue J, Epstein AJ (1991) XPS study of self-doped conducting polyaniline and parent systems. Macromolecules 24:4441–4445. https://doi.org/10.1021/ma00015a030

Yue J, Epstein AJ, Zhong Z, Gallagher PK, Macdiarmid AG (1991) Thermal stabilities of polyanilines. Synth Met 41:765–768. https://doi.org/10.1016/0379-6779(91)91180-I

Yurdakal S, Garlisi C, Özcan L, Bellardita M, Palmisano G (2019) Chapter 4 - (Photo)catalyst characterization techniques: Adsorption isotherms and BET, SEM, FTIR, UV–Vis, photoluminescence, and electrochemical characterizations. In: Marcì G, Palmisano L (eds) Heterogeneous Photocatalysis, 1st edn. Elsevier, Amsterdam, pp 87–152. https://doi.org/10.1016/B978-0-444-64015-4.00004-3

Zhang Y, Li Q, Sun L, Tang R, Zhai J (2010) High efficient removal of mercury from aqueous solution by polyaniline/humic acid nanocomposite. J Hazard Mater 175:404–409. https://doi.org/10.1016/j.jhazmat.2009.10.019